NONDESTRUCTIVE TESTING OF OVERHEAD TRANSMISSION LINES: NUMERICAL AND EXPERIMENTAL INVESTIGATION

A Thesis

by

SALIL SUBHASH KULKARNI

Submitted to the Office of Graduate Studies of
Texas A&M University
in partial fulfillment of the requirements for the degree of

MASTER OF SCIENCE

December 2009

Major Subject: Civil Engineering

NONDESTRUCTIVE TESTING OF OVERHEAD TRANSMISSION LINES: NUMERICAL AND EXPERIMENTAL INVESTIGATION

A Thesis

by

SALIL SUBHASH KULKARNI

Submitted to the Office of Graduate Studies of
Texas A&M University
in partial fulfillment of the requirements for the degree of

MASTER OF SCIENCE

Approved by:

Chair of Committee,	Stefan Hurlebaus
Members of Committee,	Jose Roesset
	Gary Gaukler
Head of Department,	John Niedzwecki

December 2009

Major Subject: Civil Engineering

ABSTRACT

Non-destructive Testing of Overhead Transmission Lines: Numerical and Experimental Investigation. (December 2009)

Salil Subhash Kulkarni, B.Tech, College of Engineering, Pune, India

Chair of Advisory Committee: Dr. Stefan Hurlebaus

Overhead transmission lines are periodically inspected using both on-ground and helicopter-aided visual inspection. Factors including sun glare, cloud cover, close proximity to power lines and the rapidly changing visual circumstances make airborne inspection of power lines a particularly hazardous task. In this research, a finite element model is developed that can be used to create the theoretical dispersion curves of an overhead transmission line. The complex geometry of the overhead transmission line is the primary reason for absence of a theoretical solution to get the analytical dispersion curves. The numerical results are then verified with experimental tests using a non-contact and broadband laser detection technique. The methodology developed in this study can be further extended to a continuous monitoring system and be applied to other cable monitoring applications, such as bridge cable monitoring, which would otherwise put human inspectors at risk.

DEDICATION

Dedicated To My Parents

ACKNOWLEDGEMENTS

I take this opportunity to acknowledge the technical guidance and financial assistance offered by Dr. Stefan Hurlebaus during the research period. I thank him for entrusting me with this prestigious research work and for helping me at all stages and through all my difficult times. I also thank him for his valuable time and promptness to clear my doubts anytime I approached him. Without him, this project would not be in its present shape.

I acknowledge all the technical assistance received from Dr. Jose Roesset. I thank him for sharing his technical expertise and for helping me improve my numerical model from time to time during the research period.

I acknowledge the timely guidance provided by Mr. Hrishikesh Sharma and all my other friends and colleagues at Texas A&M University as well as at the College of Engineering, Pune, India during this research project.

Lastly I thank my father, mother and sister for their blessings which has made this day possible. They will always continue to be my source of inspiration.

TABLE OF CONTENTS

Page

LIST OF FIGURES

Page

Page

Page

Page

LIST OF TABLES

Page

1. INTRODUCTION

Multi-strand cables are the main components of a number of structures. Some of them are the overhead transmission lines; suspension or cable stayed bridges, prestressed or post tensioned members, elevators etc. Being the main load carrying members, their efficient functioning is of highest priority. The cables can suffer defects in their functioning life that could pose a serious threat to its safe operation. This research aims at developing a method for structural health monitoring of overhead transmission lines using ultrasonic waves.

The overhead transmission line can undergo defects like broken insulators, loose earth conductors, broken strands, broken lightning rods etc. Presently and in the past, transmission line monitoring has been undertaken by both on-ground and aerial methods. The aerial approach involves using a helicopter. These inspections are also affected by the rapidly changing weather conditions. Some of these inspections have resulted in accidents, some involving human casualties as well. Table 1.1 summarizes the helicopter data for helicopter accidents during aerial inspections [1]. Figure 1.1 shows an ongoing helicopter survey while Figure 1.2 shows a helicopter accident during a transmission line investigation.

This thesis follows the style of NDT&E Journal.

Table 1.1: Summary of helicopter accidents during aerial observations.

	1997	1998	1999	2000	2001	2002	2003	2004	2005	2006
Total Accidents	163	191	197	206	182	205	214	180	193	162
Fatal Accidents	27	34	31	35	29	26	37	33	25	25
Fatal Injuries	43	66	57	63	51	41	67	68	40	43
FAR 91 Aerial	6	6	13	7	5	8	8	9	4	6

Figure 1.1: Aerial inspection of high voltage power lines.

Figure 1.2: Crash site of a helicopter involved in aerial inspection of a high voltage power line.

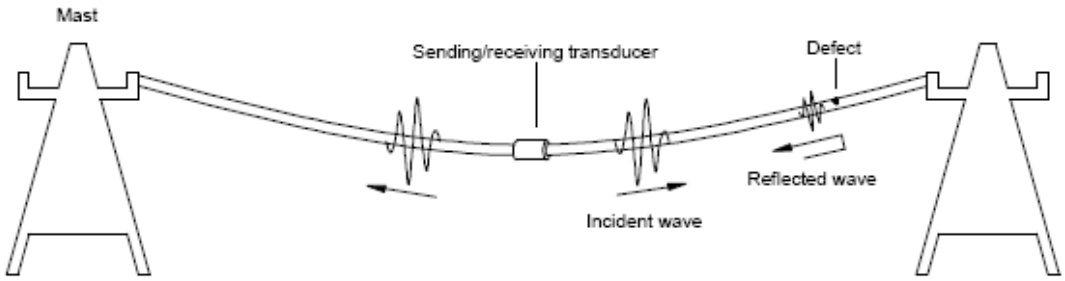

Figure 1.3: Basic idea of transmission line monitoring.

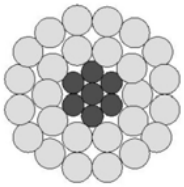

Figure 1.4: Cross-section of a transmission line.

The basic idea of this study is depicted in Figure 1.3. A piezoelectric transducer is located in the middle part of the cable. It can send as well as receive ultrasonic waves. The sent wave reflects at any defect it encounters in its path. This reflected wave reaches back the transducer. The amplitude of the reflected wave is compared to a threshold value. If it is more than the threshold value, existence of a defect can be ascertained. Amongst the various defects that can occur in a transmission line, this research specifically looks into the detection of cracks in the individual strands.

The overhead transmission line consists of a total of 33 strands. There are 26 aluminum strands each of 4.45mm in diameter and 7 steel strands of 3.5mm diameter. The steel strands are provided to carry the load of the cable. The total diameter of the cable is about 28.3mm. A cross-sectional view of the cable is shown in Figure 1.4. The experimental work looks into the attenuation and dispersion behavior of the first longitudinal mode. It is first performed for a single aluminum strand.

Use of ultrasonic waves for defect detection in cables has been a topic of previous research. However, very few have tried to extend their findings for the case of an entire cable which makes this research unique. Elastic pulse propagation in wires with circular cross-section was studied by Meitzler [2]. Based on his observations of pulse distortion for pulses propagating in other modes, he concluded that the coupling between the various modes of propagation leads to pulse distortion.

Rizzo and Lanza di Scalea [3] extended this research to seven wire cables. Ultrasonic waves in individual wires were detected using magnetostrictive sensors. Their research specifically spoke about the acoustoelastic effect in cables. The change in velocity of longitudinal waves as an effect of applied stress is called the acoustoelastic effect. They proposed an acoustoelastic formulation of the Pochhammer-Chree longitudinal vibrations in cylinder shaped waveguides. This would help in predicting the change in the velocity of the ultrasonic waves as a function of stress.

Further research by Rizzo and Lanza di Scalea [4] looked into wave propagation in seven strand cables to the extent of individual strands. This time their research was concentrated on the modes of propagation of waves that travel with minimal losses. They

characterized the longitudinal and flexural waves in terms of dispersive velocity and frequency dependent attenuation. They used a broad-band ultrasonic setup and time frequency wavelet transform processing to achieve their objective.

In another paper by Rizzo and Lanza di Scalea [5], they look at the denoising property of the Discrete Wavelet Transform (DWT).

Washer et al. [6] looked into stress levels for post-tensioning rods using acoustoelastic effect.

The technique of using artificial neural networks for monitoring overhead transmission lines was suggested by Jayasinghe et al. [7]. This technique is based on the high frequency phenomena associated with the partial discharge occurrences that originate from different defects arising in the transmission lines. A simulation technique based on the same theory was proposed by Aggarwal et al. [8].

A microprocessor based technique was proposed by Muraoka et al. [9]. The process was based on measuring the impedance to a fault point by recording the current and voltage at that location. The voltage drop per unit length can be obtained from the local terminal current and the line impedance per unit length. Using this, the location of the defect can be determined by simply taking the ratio of the line voltage drop at that location to the voltage drop per unit length.

However, none of the research done in the past on this topic attempted to use the finite element (FE) procedure for studying wave propagation in single or multi-wire cables. Most of the past research involved using the experimental methods to reach their

respective conclusions. The research was limited to the topic of studying the behavior and propagation of ultrasonic waves in cables. Moser [10] actually made use of the FE method for studying wave propagation in solids. However, the solid he chose was a simple plate. Compared to the multi-wire strand, the geometry of the plate is relatively very simple to model. Further the element size for the mesh depends on the frequency of the propagating wave. Moser used a lower frequency which allowed him to use a coarser mesh and still get good results. However, the frequency under consideration for this research requires a much finer mesh which further complicates the situation.

Protopappas et al. [11] studied the use of ultrasonic waves in the intact and healing long bones. The bone healing process was simulated as a three stage process by constructing a finite element model of the fracture callus. The model is subjected to a broadband 1-MHz excitation and the dispersion of guided modes is compared to the analytical dispersion curves.

Another important aspect which separates this research from earlier work is the fact that all earlier work involved simple geometries which already had existing analytical solutions. For the multi-strand cable, there is no analytical solution.

This thesis is divided into six sections. Section 2 discusses the theory behind guided waves in circular rods. It includes details about longitudinal modes, flexural modes and dispersion curves. Section 3 explains the experimental characterization of the different modes and talks about the experiments performed to study the propagation of ultrasonic waves in overhead transmission lines. The finite element model developed to

corroborate the experimental results is discussed in Section 4. Section 5 presents a discussion on the results obtained which is then followed by conclusions in Section 6.

2. GUIDED WAVES IN CIRCULAR RODS

Ultrasonic waves are used for material characterization in many structural health monitoring and nondestructive evaluation applications. Guided ultrasonic waves are particularly effective in interrogating large structural components, because guided waves propagate far distances when compared to body waves. Guided waves appear in a medium that has two parallel surfaces in relative proximity. The disturbances are constrained to move between these two surfaces and therefore the system behaves as a waveguide. One considers two generic cases which can be called symmetric and antisymmetric, respectively; former is approximately rod-like or longitudinal while the latter is approximately beam-like or flexural. The essence of the analysis is that standing waves are established in the transverse (short) direction while the propagating waves are manifested in the longitudinal direction. The following equations are derived according to [12].

Consider a solid, circular, cylindrical rod as shown in Figure 2.1. The components of the displacements can be written in terms of potential functions in cylindrical coordinates

$$\begin{aligned} u_r &= \frac{\partial \Phi}{\partial r} - \frac{1}{r}\frac{\partial H_z}{\partial \theta} - \frac{\partial H_\theta}{\partial z} \\ u_\theta &= \frac{1}{r}\frac{\partial \Phi}{\partial \theta} + \frac{\partial H_r}{\partial z} - \frac{\partial H_z}{\partial r} \\ u_z &= \frac{\partial \Phi}{\partial z} + \frac{1}{r}\frac{\partial \left(rH_\theta\right)}{\partial r} - \frac{1}{r}\frac{\partial H_r}{\partial \theta}, \end{aligned} \tag{2.1}$$

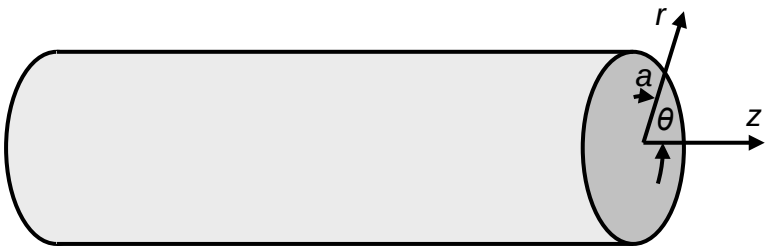

Figure 2.1: Coordinates for a solid cylindrical rod.

where u_r, u_z, u_θ are the displacements in cylindrical co-ordinates and Φ, H are the potential functions.

The potentials Φ and $\mathbf{H}$ satisfy the scalar and vector equations,

$$\nabla^2\Phi = \frac{1}{c_1^2}\frac{\partial^2\Phi}{\partial t^2}, \qquad \nabla^2\mathbf{H} = \frac{1}{c_2^2}\frac{\partial^2\mathbf{H}}{\partial t^2}, \tag{2.2}$$

where,

$$\nabla^2\Phi = \frac{\partial^2\Phi}{\partial r^2} + \frac{1}{r}\frac{\partial\Phi}{\partial r} + \frac{1}{r^2}\frac{\partial^2\Phi}{\partial\theta^2} + \frac{\partial^2\Phi}{\partial z^2}, \tag{2.3}$$

$$\nabla^2\mathbf{H} = \begin{pmatrix} \nabla^2 H_r - \dfrac{H_r}{r^2} - \dfrac{2}{r^2}\dfrac{\partial H_\theta}{\partial\theta} \\ \nabla^2 H_\theta - \dfrac{H_\theta}{r^2} + \dfrac{2}{r^2}\dfrac{\partial H_r}{\partial\theta} \\ \nabla^2 H_z \end{pmatrix}. \tag{2.4}$$

The stresses are given by Hooke's Law, $\tau_{ij} = \lambda \Delta \delta_{ij} + 2\mu e_{ij}$, where,

$$
\begin{aligned}
e_{rr} &= \frac{\partial u_r}{\partial r}, \\
e_{\theta\theta} &= \frac{1}{r}\frac{\partial u_\theta}{\partial \theta} + \frac{u_r}{r}, \\
e_{zz} &= \frac{\partial u_z}{\partial r}, \\
e_{r\theta} &= \frac{1}{2}\left(\frac{1}{r}\frac{\partial u_r}{\partial \theta} + \frac{\partial u_\theta}{\partial r} - \frac{\partial u_\theta}{\partial r} \right), \\
e_{rz} &= \frac{1}{2}\left(\frac{1}{r}\frac{\partial u_z}{\partial r} + \frac{\partial u_r}{\partial z} \right), \\
e_{\theta z} &= \frac{1}{2}\left(\frac{\partial u_\theta}{\partial z} + \frac{1}{r}\frac{\partial u_z}{\partial \theta} \right).
\end{aligned}
\tag{2.5}
$$

The boundary conditions for the problem will be given by

$$
\tau_{rr}(r=a) = \tau_{r\theta}(r=a) = \tau_{rz}(r=a) = 0 \tag{2.6}
$$

One can consider now the conditions under which harmonic waves may propagate in a cylinder. Thus consider Φ, H_r to be of the general form

$$
\begin{aligned}
\Phi &= f(r)\Theta_\phi(\theta)\mathrm{e}^{i(\xi z - \omega t)}, \\
H_r &= h_r(r)\Theta_r(\theta)\mathrm{e}^{i(\xi z - \omega t)}.
\end{aligned}
\tag{2.7}
$$

When these are substituted in the scalar and vector wave equations, sine and cosine solutions results for the θ-dependence. Thus for Φ one obtains

$$
f''\Theta_\phi + \frac{1}{r} f'\Theta_\phi + \frac{1}{r^2} f'\Theta''_\phi - \xi^2 f\Theta_\phi = -\frac{\omega^2}{c_1^2} f\Theta_\phi, \tag{2.8}
$$

giving

$$r^2\frac{f''}{f}+r\frac{f'}{f}-\left(\xi^2-\frac{\omega^2}{c_1^2}\right)r^2=-\frac{\Theta_\phi''}{\Theta_\phi}=k^2. \tag{2.9}$$

Thus,

$$\Theta_\phi = A\sin k\theta + B\cos k\theta. \tag{2.10}$$

Single valuedness requirements on Θ_ϕ make $k=n$, an integer. Similar solutions also hold for $\Theta_r,\Theta_\theta,\Theta_z$. Furthermore, later requirements on the nature of the θ dependence for the longitudinal and flexural modes would lead to discard either sine or cosine terms in the various Θ results. The resulting expressions for Φ, H_r, H_θ, H_z become

$$\begin{aligned}
\Phi &= f(r)\cos n\theta \mathrm{e}^{i(\xi z-\omega t)},\\
H_r &= h_r(r)\sin n\theta \mathrm{e}^{i(\xi z-\omega t)},\\
H_\theta &= h_\theta(r)\cos n\theta \mathrm{e}^{i(\xi z-\omega t)},\\
H_z &= h_z(r)\sin n\theta \mathrm{e}^{i(\xi z-\omega t)}.
\end{aligned} \tag{2.11}$$

One now proceeds with the determination of the r dependence for the four functions. Starting with Φ, equation (2.10) yields

$$\frac{\mathrm{d}^2 f}{\mathrm{d}r^2}+\frac{1}{r}\frac{\mathrm{d}f}{\mathrm{d}r}+\left(\alpha^2-\frac{n^2}{r^2}\right)f=0, \tag{2.12}$$

where, $\alpha^2=\omega^2/c_1^2-\xi^2$. This is Bessel's equation of order *n* having the solution

$$f(r)=AJ_n(\alpha r), \tag{2.13}$$

where the second solution $Y_n(\alpha r)$ has been discarded because of its singular behavior at the origin. The equation that results for h_z is similar to (2.12) with α^2 replaced by β^2.

The solution is

$$h_z(r) = B_3 J_n(\beta r), \tag{2.14}$$

where, $\beta^2 = \omega^2 / c_2^2 - \xi^2$. The remaining two equations $h_r(r)$ and $h_\theta(r)$ will be coupled, as study of the vector Laplacian (2.4) will reveal. The resulting equations are

$$\begin{aligned}
&\frac{\mathrm{d}^2 h_r}{\mathrm{d}r^2} + \frac{1}{r}\frac{\mathrm{d}h_r}{\mathrm{d}r} + \frac{1}{r^2}\left(-n^2 h_r + 2n h_\theta - h_r\right) - \xi^2 h_r + \frac{\omega^2}{c_2^2} h_r = 0, \\
&\frac{\mathrm{d}^2 h_\theta}{\mathrm{d}r^2} + \frac{1}{r}\frac{\mathrm{d}h_\theta}{\mathrm{d}r} + \frac{1}{r^2}\left(-n^2 h_\theta + 2n h_r - h_\theta\right) - \xi^2 h_\theta + \frac{\omega^2}{c_2^2} h_\theta = 0.
\end{aligned} \tag{2.15}$$

These equations may be solved simultaneously for h_r and h_θ. Thus subtract the first from the second to give

$$\left\{\frac{\mathrm{d}^2}{\mathrm{d}r^2} + \frac{1}{r}\frac{\mathrm{d}}{\mathrm{d}r} + \beta^2 - \frac{(n+1)^2}{r^2}\right\}(h_r - h_\theta) = 0. \tag{2.16}$$

This has the solution

$$h_r - h_\theta = 2B_2 J_{n+1}(\beta r). \tag{2.17}$$

Add the two equations of (2.15) to give

$$\left\{\frac{\mathrm{d}^2}{\mathrm{d}r^2}+\frac{1}{r}\frac{\mathrm{d}}{\mathrm{d}r}+\beta^2-\frac{(n-1)^2}{r^2}\right\}(h_r+h_\theta)=0. \tag{2.18}$$

This has the solution

$$h_r+h_\theta=2B_1J_{n-1}(\beta r). \tag{2.19}$$

Adding and subtracting (2.17) and (2.18), one obtains

$$\begin{aligned} h_r &= B_1J_{n-1}(\beta r)+B_2J_{n+1}(\beta r),\\ h_\theta &= B_1J_{n-1}(\beta r)-B_2J_{n+1}(\beta r). \end{aligned} \tag{2.20}$$

There are four constants associated with the components of displacement, with three boundary conditions to be applied. The property of gauge in variance can now be used to eliminate one of the constants, without loss of generality. Setting $B_2=0$, which results in $h_r(r)=-h_\theta(r)$, the resulting displacements and some of the stresses are

$$\begin{aligned} u_r &= \{f'+(n/r)h_z+\xi h_r\}\cos n\theta \mathrm{e}^{i(\xi z-\omega t)},\\ u_\theta &= \{-(n/r)f+\xi h_r-h_z'\}\sin n\theta \mathrm{e}^{i(\xi z-\omega t)},\\ u_z &= \{-\xi f-h_r'-(n+1)h_r/r\}\cos n\theta \mathrm{e}^{i(\xi z-\omega t)}, \end{aligned} \tag{2.21}$$

$$\begin{aligned} \tau_{rr} &= \left[-\lambda(\alpha^2+\xi^2)f+2\mu\left\{f''+\frac{n}{r}\left(h_z'-\frac{h_z}{r}\right)+\xi h_r'\right\}\right]\cos n\theta \mathrm{e}^{i(\xi z-\omega t)},\\ \tau_{r\theta} &= \mu\left[-\frac{2n}{r}\left(f'-\frac{f}{r}\right)-(2h_z''-\beta^2h_z)-\xi\left(\frac{n+1}{r}h_r-h_r'\right)\right]\sin n\theta \mathrm{e}^{i(\xi z-\omega t)},\\ \tau_{rz} &= \mu\left[-2\xi f'-\frac{n}{r}\left\{h_r'+\left(\frac{n+1}{r}-\beta^2+\xi^2\right)h_r\right\}-\frac{n\xi}{r}h_z\right]\cos n\theta \mathrm{e}^{i(\xi z-\omega t)}. \end{aligned} \tag{2.22}$$

The procedure to obtain the frequency equation is to substitute the results for f, h_r, h_θ, h_z in (2.22) evaluated at $r = a$. The resulting determinant of coefficients, which yields the frequency equation, is

$$a_{ij} = 0 \qquad (i, j = 1,2,3), \tag{2.23}$$

where,

$$\begin{aligned}
a_{11} &= \left\{ \frac{\lambda\left(\alpha^2 + \xi^2\right)(\alpha a)^2}{2\mu\alpha^2} + (\alpha a)^2 - n^2 \right\} J_n(\alpha a) + \alpha a \, J_n'(\alpha a), \\
a_{12} &= \left\{ n^2 - (\beta a)^2 \right\} J_n(\beta a) - \beta a \, J_n'(\beta a), \\
a_{13} &= 2n\left\{ \beta a \, J_n'(\beta a) - J_n(\beta a) \right\}, \\
a_{21} &= n\left\{ \alpha a \, J_n'(\alpha a) - J_n(\alpha a) \right\}, \\
a_{22} &= -n\left\{ \beta a \, J_n'(\beta a) - J_n(\beta a) \right\}, \\
a_{23} &= -\left\{ 2n^2 - (\beta a)^2 \right\} J_n(\beta a) + 2\beta a \, J_n'(\beta a), \\
a_{31} &= -\alpha a J_n'(\alpha a), \\
a_{32} &= -\frac{\beta^2 - \xi^2}{2\xi^2} \beta a J_n'(\beta a), \\
a_{33} &= n J_n(\beta a).
\end{aligned} \tag{2.24}$$

2.1 LONGITUDINAL MODES

Consider the propagation when $u_\Theta = \partial / \partial\Theta = 0$. From equation (2.2), one has

$$u_r = \frac{\partial \Phi}{\partial r} - \frac{\partial H_\theta}{\partial z}, \tag{2.25}$$

$$u_z = \frac{\partial \Phi}{\partial z} + \frac{1}{r}\frac{\partial (rH_\theta)}{\partial r}. \tag{2.26}$$

So, that determination of Φ and H_θ shall be sufficient to prescribe the motion. The solutions for Φ and H_θ have been given previously by (2.11), where $n = 0$ in the $\cos n\theta$ dependence. Thus it follows that

$$\Phi = AJ_0(\alpha r)\mathrm{e}^{\mathrm{i}(\xi z - \omega t)}, \tag{2.27}$$

$$H_\theta = -B_2 J_1(\beta r)\mathrm{e}^{\mathrm{i}(\xi z - \omega t)}. \tag{2.28}$$

Substitution of the above in the non-trivial boundary conditions, which are $\tau_{rr}(r = a) = 0$ and $\tau_{rz}(r = a) = 0$ yields the frequency equation. This is given in a cofactor matrix

$$\begin{vmatrix} a'_{11} & a'_{12} \\ a'_{31} & a'_{32} \end{vmatrix} = 0, \tag{2.29}$$

where,

$$\begin{aligned}
a'_{11} &= \left\{ \frac{\lambda(\alpha^2 + \xi^2)(\alpha a)^2}{2\mu\alpha^2} + (\alpha a)^2 \right\} J_0(\alpha a) + \alpha a \; {}'_0(\alpha a), \\
a'_{12} &= -(\beta a)^2 J_0(\beta a) - \beta a \; {}'_0(\beta a), \\
a'_{31} &= -\alpha a J'_0(\alpha a), \\
a'_{32} &= -\frac{\beta^2 - \xi^2}{2\xi^2}\beta a J'_0(\beta a).
\end{aligned} \tag{2.30}$$

It expands to give

$$\frac{2\alpha}{a}\left(\beta^2+\xi^2\right)J_1(\alpha a)J_1(\beta a)-\left(\beta^2-\xi^2\right)J_0(\alpha a)J_1(\beta a)-4\xi^2\alpha\beta J_1(\alpha a)J_0(\beta a)=0. \tag{2.31}$$

This result is referred to as the Pochhammer frequency equation for the longitudinal modes. The displacements for this mode are given by

$$\begin{aligned} u_r &= B_2\left\{-\frac{A}{B_2}\alpha J_1(\alpha r)+i\xi J_1(\beta r)\right\}\mathrm{e}^{i(\xi z-\omega t)}, \\ u_z &= B_2\left\{\frac{A}{B_2}i\xi J_0(\alpha r)-\beta J_0(\beta r)\right\}\mathrm{e}^{i(\xi z-\omega t)}, \end{aligned} \tag{2.32}$$

where,

$$\frac{A}{B_2}=-\left(\frac{\alpha}{\beta}\right)^2\frac{\beta^2-\xi^2}{2\xi^2}\frac{J_1(\beta a)}{J_1(\alpha a)}. \tag{2.33}$$

The interpretation of the displacement fields as being a resultant of dilatational and shear waves holds. Thus in the case of u_z the $J_0(\alpha r)$ term of (2.32) may be interpreted as the longitudinal component of a set of plane dilatational waves whose normals form a conical surface, where the axis of the cone is the z-axis. The $J_0(\beta r)$ term of (2.32) is the longitudinal component of a set of transverse waves.

2.2 FLEXURAL MODES

The general characteristic equation (2.23) was found to yield the longitudinal frequency equation for $n=0$. For this case one or two of the displacement components were found to vanish. In order to investigate the propagation of flexural waves, all displacement

components will exist. The case of $n=1$ corresponds to the lowest order family of flexural modes. The displacements are given from (2.21) and the frequency equation is obtained by expanding (2.23). The resulting Pochhammer frequency equation is

$$J_1(\alpha a)J_1^2(\beta a)\left[f_1\frac{\beta^2a^2J_0^2(\beta a)}{J_1^2(\beta a)}+f_2\frac{\alpha\beta a^2J_0(\alpha a)J_0(\beta a)}{J_1(\alpha a)J_1(\beta a)}+f_3\frac{\beta aJ_0(\beta a)}{J_1(\beta a)}+f_4\frac{\alpha aJ_0(\alpha a)}{J_1(\alpha a)}+f_5\right]=0, \tag{2.34}$$

where,

$$\begin{aligned}
f_1 &= 2\left(\beta^2a^2-\xi^2a^2\right)^2,\\
f_2 &= 2\beta^2a^2\left(5\xi^2a^2+\beta^2a^2\right),\\
f_3 &= \beta^6a^6-10\beta^4a^4-2\beta^4\xi^2a^6+2\beta^2\xi^2a^4+\beta^2\xi^4a^6-4\xi^4a^4,\\
f_4 &= 2\beta^2a^2\left(2\beta^2\xi^2a^4-\beta^2a^2-9\xi^2a^2\right),\\
f_5 &= \beta^2a^2\left(-\beta^4a^4+\beta^2a^2-2\beta^2\xi^2a^4+8\xi^2a^2-\xi^4a^4\right).
\end{aligned} \tag{2.35}$$

2.3 DISPERSION CURVES

The theoretical solution for dispersion curves can be obtained by solving (2.31) and (2.34). Figure 2.2 shows the dispersion curves in the (f,ξ)-domain for the longitudinal and flexural waves in the frequency-wavenumber domain for an aluminum rod with diameter of 4.45 mm, together with the mode notation (L for longitudinal and F for flexural). The frequency-wavenumber domain is the most natural way to present the dispersion curves. Unfortunately, by measuring waves one obtains the propagation time. The expected arrival time t for a specific mode at circular frequency ω is given by

$$t=\frac{s}{c_g(\omega)}, \tag{2.36}$$

where, s is the source-receiver distance.

The group velocity for each of the different modes at all relevant frequencies are determined by numerically differentiating ω with respect to ξ

$$c_g = \frac{\mathrm{d}\omega}{\mathrm{d}\xi}. \tag{2.37}$$

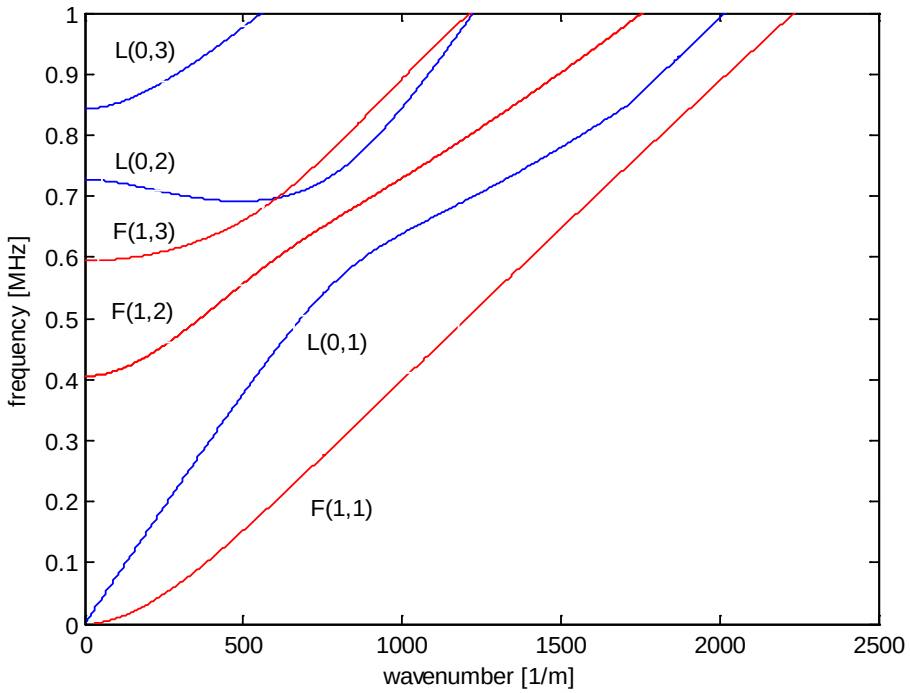

Figure 2.2: Frequency spectrum for the longitudinal (blue) and flexural (red) modes of a rod.

It is crucial that the original frequency-wavenumber domain dispersion curves are computed with a high precision. This accuracy is required in order to avoid severe numerical oscillations for the computed group velocities. The group velocity is the velocity of the energy transport (Hurlebaus, 2005) and should not be mixed up with the phase velocity.

The definition of the phase velocity is

$$c_p = \frac{\omega}{\xi}. \tag{2.38}$$

Figure 2.3 shows the first two dispersion curves for the longitudinal and flexural waves in the phase-velocity-frequency domain, while Figure 2.4 depicts these curves in the group-velocity-frequency domain. It is obvious from Figure 2.4 that longitudinal waves having a frequency below $f \sim 100$ kHz only the lowest order, or bar mode, will propagate in the strand and this mode propagates approximately non-dispersively with velocity $c = \sqrt{E/\rho}$.

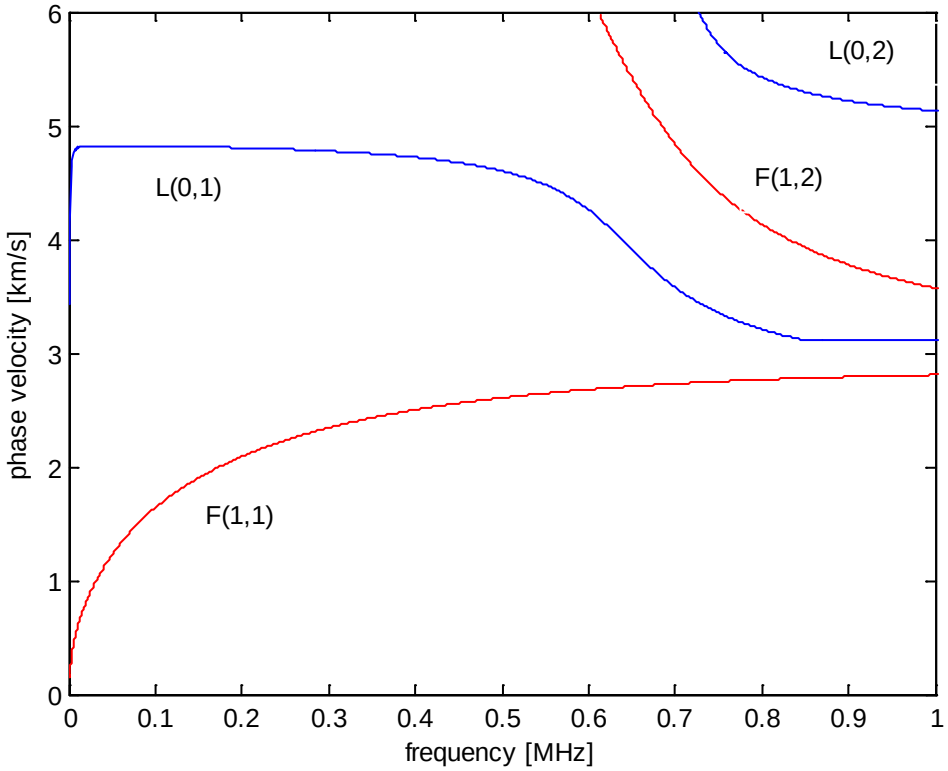

Figure 2.3: Phase velocity for the longitudinal (blue) and flexural (red) modes of a rod.

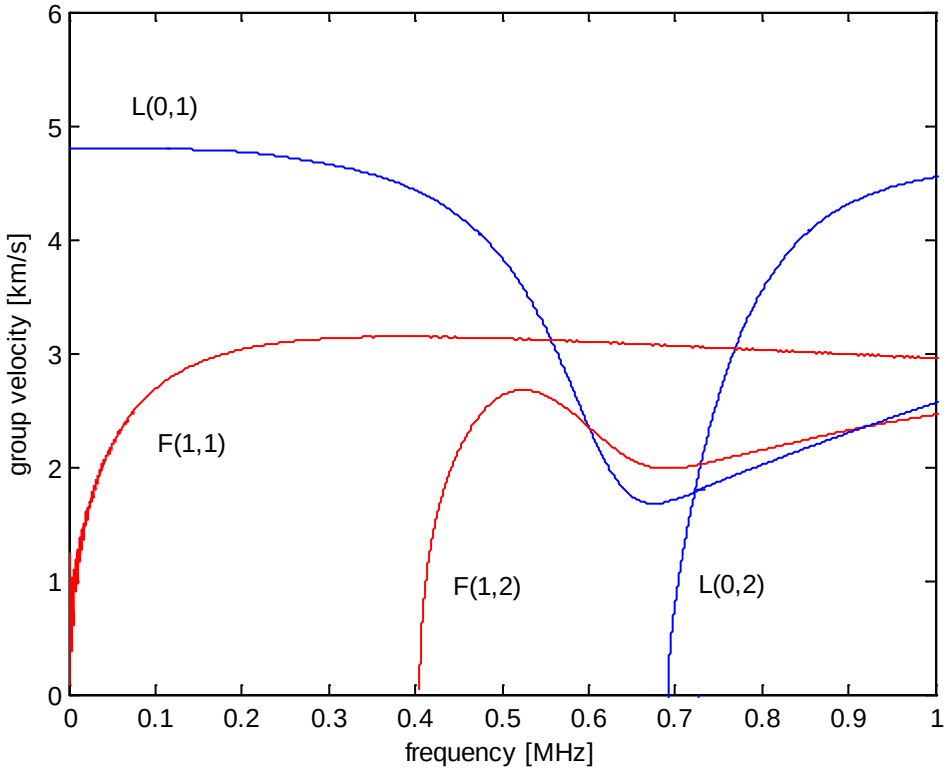

Figure 2.4: Group velocity for the longitudinal (blue) and flexural (red) modes of a rod.

3. EXPERIMENTAL CHARACTERIZATION

The previous section demonstrated the propagation of different modes in a rod. Since there exists no closed form analytical solution of the wave propagation in a wire consisting of several strands, the preliminary studies described in this section concentrates on wave propagation in a single strand.

3.1 LONGITUDINAL AND FLEXURAL MODES

The first step of this research involved determining how ultrasonic waves propagate. The experimental setup for measuring the longitudinal modes in a single strand is depicted in Figure 3.1. A single burst sine wave of a function generator is amplified with a RF amplifier and this signal is used to drive a piezoelectric transducer. The piezoelectric transducer generates an elastic wave in the strand. The wave then propagates through the aluminum strand (diameter 4.45 mm, length 820 mm), is detected by a laser vibrometer, and is captured by a digital phosphor oscilloscope.

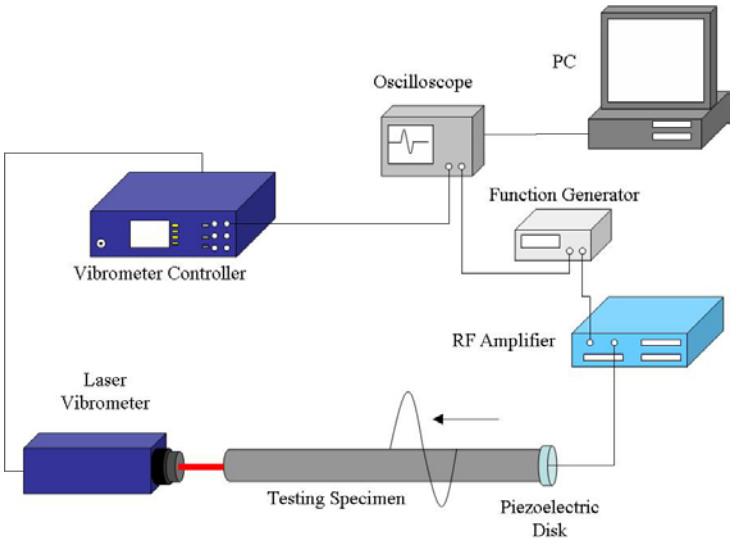

Figure 3.1: Experimental setup for longitudinal wave measurements in a single strand.

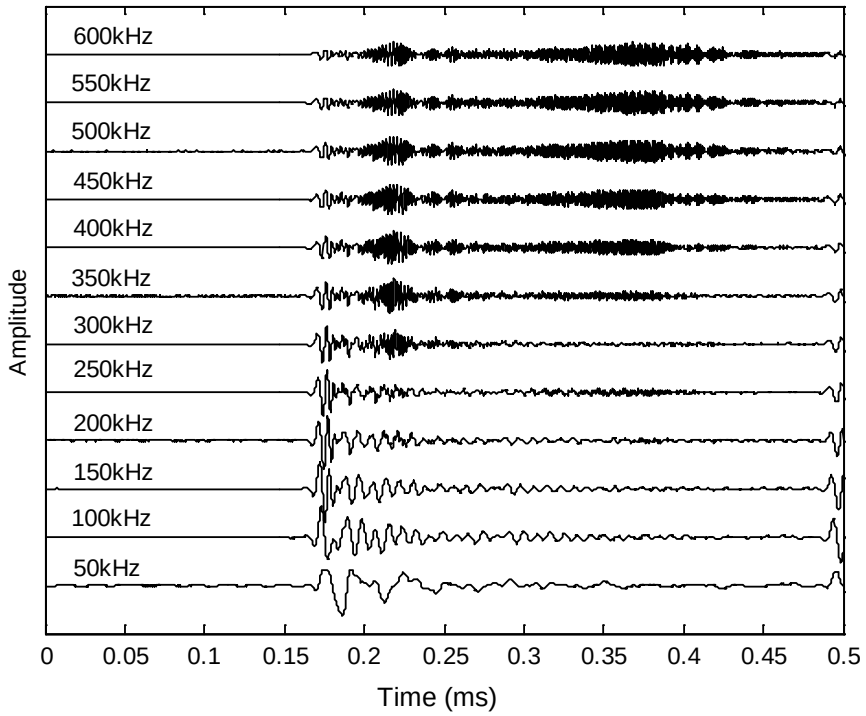

Figure 3.2: Longitudinal wave measurements in a single strand at various frequencies.

Finally, the data sets are transferred via RS232 to the PC. Note that the laser vibrometer makes non-contact, high fidelity, and point-like measurements over a wide frequency range. Figure 3.2 depicts the measured longitudinal out-of-plane velocity at the end of the strand for different excitation frequencies. It is obvious that different modes are present in the strand as already predicted in Section 2. Furthermore, it is obvious that different modes appear and disappear with frequency.

Figure 3.3, shows the equivalent results to Figure 3.2 as obtained from the finite element model of a single strand. Figure 3.4 depicts a similar setup as already shown for the measurement of the longitudinal waves; however, the laser vibrometer now measures the flexural out-of-plane velocity.

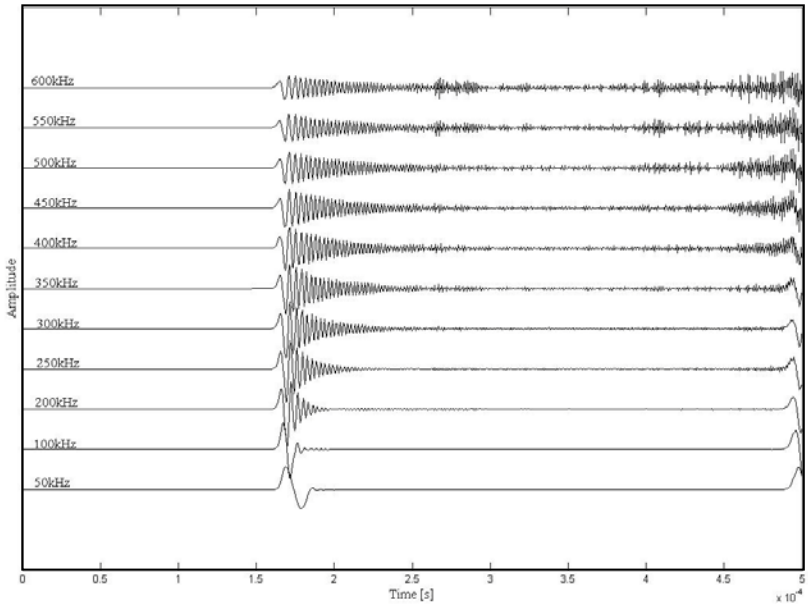

Figure 3.3: Longitudinal wave measurements in a single strand at various frequencies obtained for the finite element model.

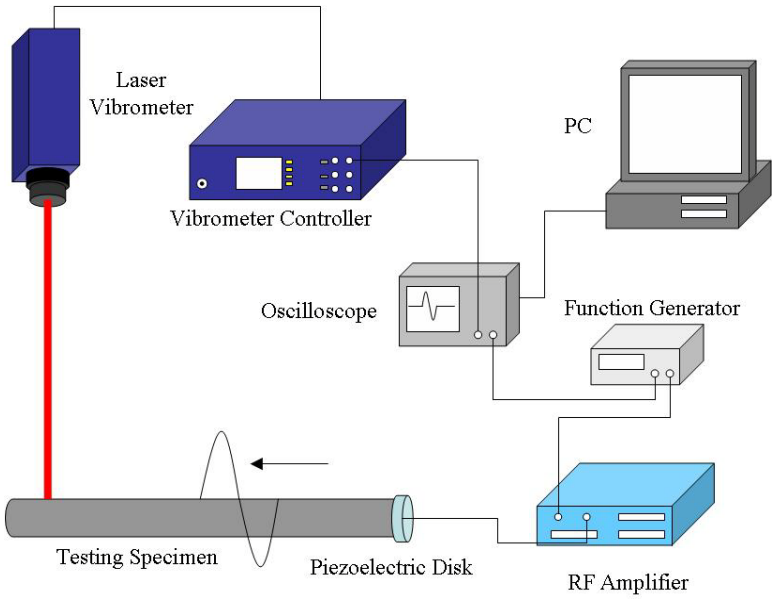

Figure 3.4: Experimental setup for flexural wave measurements in a single strand.

3.2 ATTENUATION COEFFICIENT

Considering equation (2.32) it is obvious that the amplitude of the wave does not change with distance z. Hence, this equation does not account for any attenuation due to material or geometrical effects. Therefore, one can simplify equation (2.32) by considering a constant amplitude, but adding a term that counts attenuation due to material damping

$$u_z = Ce^{i\left(\xi^* z - \omega t\right)}, \tag{3.1}$$

where C is the amplitude, ω is the frequency, and $\xi^* = \xi_1 + i\xi_2$ is the complex wave number of the propagating wave. The ξ_1 contribution is associated with propagation of the wave, and the ξ_2 contribution is associated with spatial attenuation of the wave. From equation (3.1), it follows that the ratio of the displacement amplitudes between two measurement points is

$$\frac{u_z(z+\Delta z)}{u_z(z)} = \mathrm{e}^{-\xi_2 \Delta z}, \tag{3.2}$$

where Δz is the separation distance between the measurement points. Rearranging for the attenuation coefficient ξ_2 yields

$$\xi_2 = \frac{1}{\Delta z} \ln\left(\frac{u_z(z)}{u_z(z+\Delta z)} \right). \tag{3.3}$$

Instead of measuring at the surface of the strand at two different points, one can use the same experimental setup as described in Figure 3.1. The laser Doppler vibrometer is particularly well suited to such attenuation measurements since it is non-contact and therefore does not influence wave propagation. Since the wave is bouncing back and forth it is possible to get multiple reflections. The maximum amplitudes of the reflections can be used to calculate the attenuation coefficient simply by replacing Δz with twice of the integer of the length of the strand. Substituting the measured amplitudes and the separation distance into equation (3.3) yields an experimental estimate for the attenuation coefficient. Figure 3.5 shows the multiple reflections of the longitudinal wave in a single aluminum strand (diameter of 4.45 mm, length of 820 mm),

for a single burst excitation of frequency 100 kHz. By assuming a reasonable signal to noise ratio SNR=2, it can be seen that the longitudinal wave propagates a very long distance. The amplitude of the wave exceeds the signal to noise ratio of two even after propagating over 30 m. The attenuation coefficient of the first longitudinal mode at this specific excitation frequency can be obtained as $\xi_2 = 0.15$ 1/m.

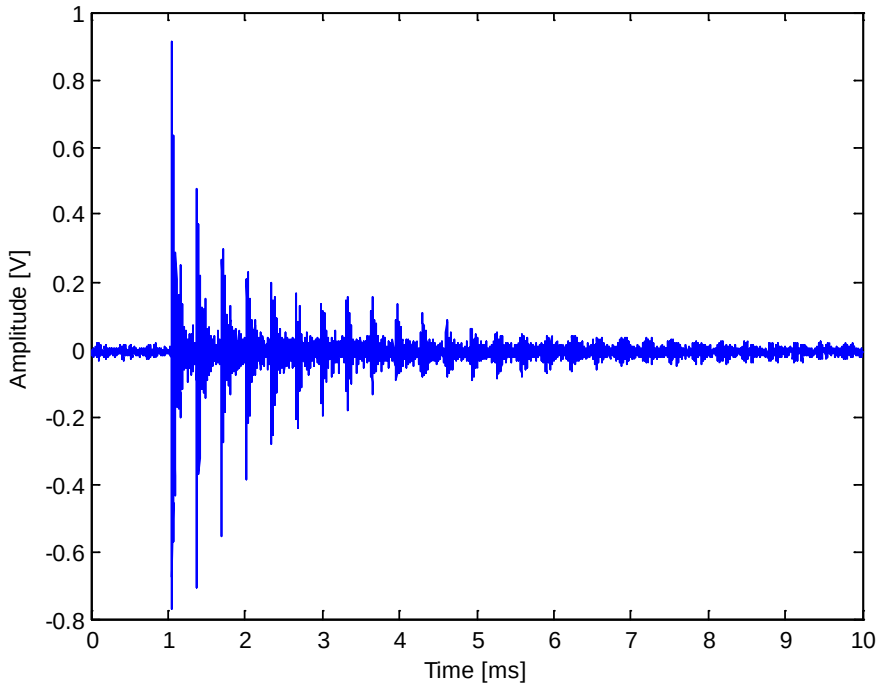

Figure 3.5: Longitudinal wave in a strand with multiple reflections.

3.3 DAMAGE DETECTION

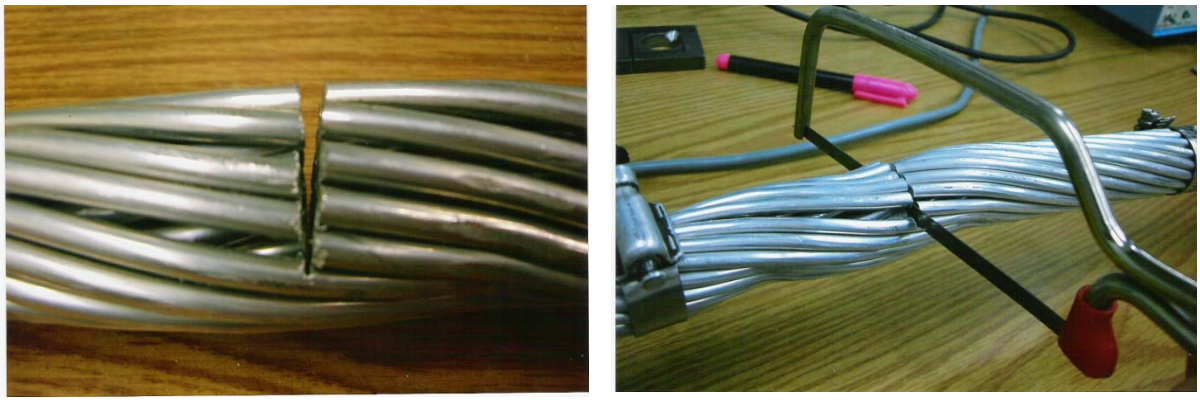

Figure 3.6: View of transverse cut in the cable.

Since the overall goal of this research is to monitor overhead transmission lines, artificial damage in the form of a transverse cut has to be inflicted on the cable. Cuts are made into the wire (Figure 3.6) at 700 mm from the piezoelectric ring using a handsaw and data is collected at different levels of damage ranging from a 2 mm cut to a complete cut. The same experimental setup is used as already described in the previous section.

In the signals received, the original reflections that existed before cutting occurred due to the waves propagating back off the end of the specimen and reflections due to the cut could both be seen. With increasing depth of the cut, the amplitudes of the reflections from the end become smaller while the reflections due to the cut increase in amplitude. Figure 3.7 depicts a signal of the undamaged cable as well as of the cable where depth of the cut is 7 mm. Figure 3.8 is a zoom of Figure 3.7 and it additionally shows the reflection due to a complete cut.

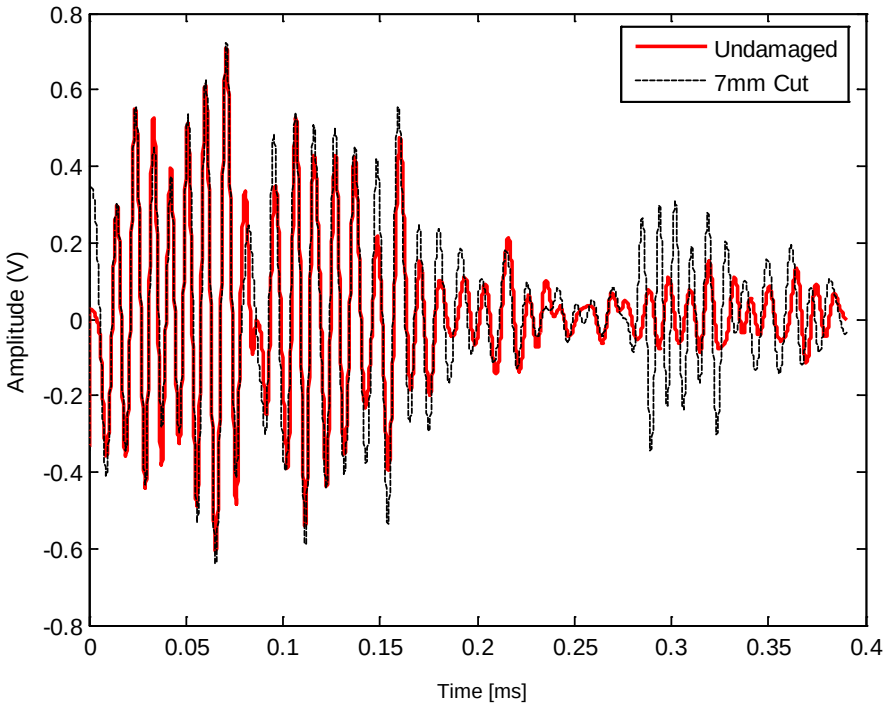

Figure 3.7: Change in signal due to damage.

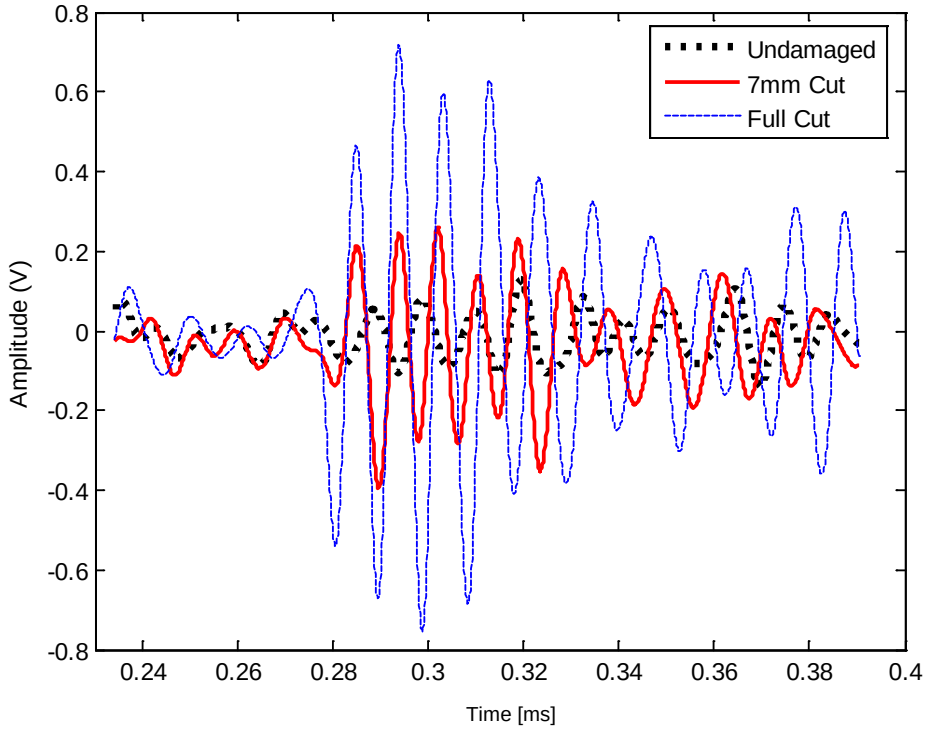

Figure 3.8: Zoom of the reflected signal.

Once the cable was cut into two pieces, the final signal resembled the original signal of the wire before cutting occurred. The only difference that existed between the signals was the location between reflections. When the transmission line is cut into two pieces, the distance between reflections is shorter due to the smaller length of the cable. It is important to note that the signal amplitude is not zero at the undamaged cable because of the multi-mode behavior of the wave. So, for monitoring of overhead transmission lines, one always has to compare the undamaged cable with the damaged one. Figure 3.9 depicts the relation between the maximum amplitude of the reflected wave at the cut and the depth of the cut. It is obvious that with increasing cut the

amplitude of the reflected wave increases. As the degree of damage is increased by making deeper cuts, the maximum wave amplitude also increased and the pattern of increase follows a near linear trend. This relation can be used for monitoring purposes in order to identify the state of damage in a cable by measuring the amplitude of the reflected wave of the cable.

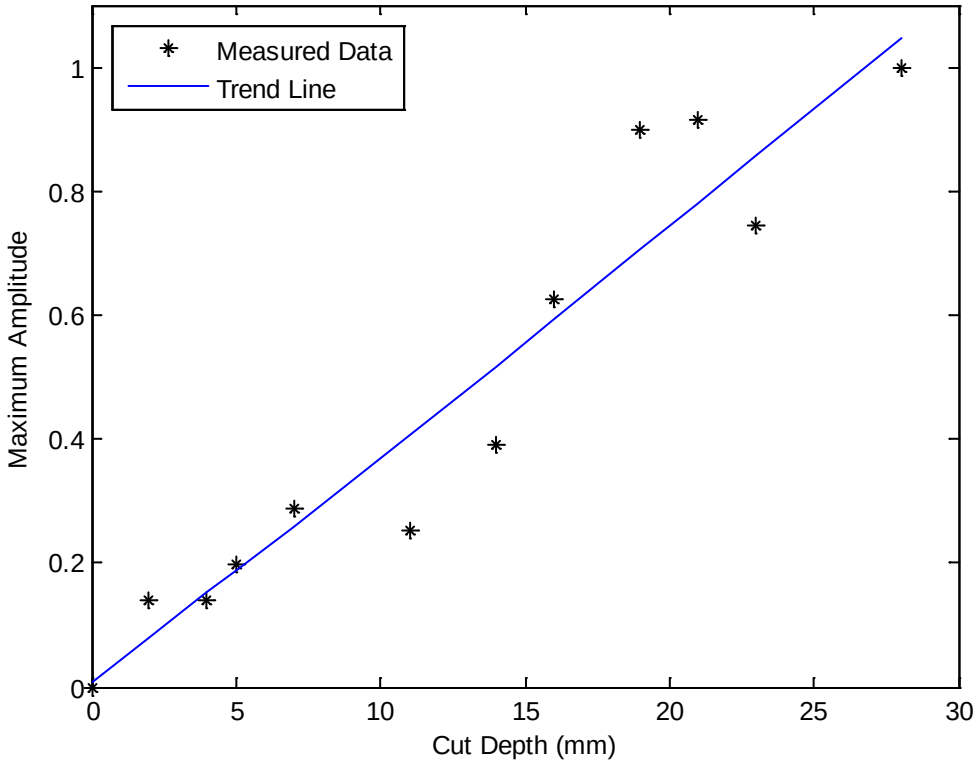

Figure 3.9: Maximum amplitude of reflected wave at various damage levels.

4. FINITE ELEMENT MODEL

This research proposes the use of ultrasonic waves for defect detection in overhead transmission lines. The finite element model is proposed to validate the procedure. As explained in Section 1, the geometry of the transmission cable is complex. It consists of a total of 33 strands (7 steel and 26 aluminum). These strands are arranged in layers and twisted together. However, along with the twists, the fact that adjacent layers of strands are twisted in opposite directions also adds to the complexity of the geometry.

The finite element modeling is done using the commercially available finite element software Abaqus. Since the problem involves studying the behavior of ultrasonic waves in a transmission cable, it is classified as a dynamic analysis. Abaqus provides two main types of dynamic analysis – the dynamic/implicit and the dynamic/explicit analysis. Abaqus/Standard uses the implicit Hilber-Hughes-Taylor operator for integration of the equations of motion while Abaqus/Explicit uses the central-difference operator. The implicit dynamic analysis requires the inversion of the integration operator matrix and solving a set of nonlinear equilibrium equations at each time increment. Comparing this with an explicit dynamic analysis where displacements and velocities are calculated in terms of quantities known at the beginning of an increment thereby eliminating the task of forming and inverting the global mass matrix which thus makes the increment relatively inexpensive compared to that of an implicit analysis [13]. However, as mentioned before, the implicit analysis uses the Hilber-Hughes-Taylor operator which is unconditionally stable while the central-difference operator used by the explicit analysis

is only conditionally stable. This advantage of the implicit analysis allows it to have no limits on the size of the time increment that can be used for the analysis.

The largest time increment that can be used by the central-difference method without rapidly growing errors has a direct relation with the time required for a stress wave to cross the smallest element in the model. This means that the time of increment in an explicit analysis will be very short if the mesh is very fine. Abaqus recommends this method over the implicit analysis for problems involving wave propagation studies.

One of the drawbacks of the explicit analysis in Abaqus/Explicit is the fact that it offers fewer element types than Abaqus/Standard. Only 1st order displacement method elements are allowed and each degree of freedom in the model must have mass or rotary inertia associated with it. However, the method has some important advantages:

1. The relation between rise in cost and problem size is linear in case of the explicit analysis whereas the cost of solving nonlinear equations rises nonlinearly with the size of the problem. Therefore Abaqus/Explicit is more suited for larger problems.
2. Processes or events that are extremely discontinuous are better handled by the explicit method as compared to the implicit method.
3. Abaqus/Explicit is better at solving general three-dimensional contact problems involving deformable bodies.
4. Stress wave propagation problems are solved more efficiently by the Abaqus/Explicit than Abaqus/Standard.

The model is subjected to loading in the form of a pulse as shown Figure 4.1. The pulse width is varied from about 1μs to 100μs. However, since there is no appreciable

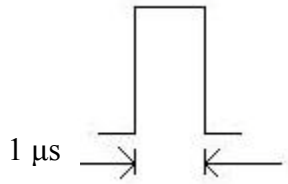

Figure 4.1: Excitation pulse.

difference in the output, the results provided through this document are for the 1μs pulse unless mentioned otherwise. The simulation runs for a total time period of 1e-04s. The outputs recorded through the simulations are the spatial velocities in the global X, Y and Z directions.

4.1 FINITE ELEMENT MODEL PARAMETERS

A stepwise approach is adopted during the modeling process. The model of an aluminum strand is developed having a length of 100mm and a diameter of 4.45mm. The main focus of this section is to look at the different stages of the modeling approach adopted.

As mentioned in the initial parts of this section, the geometry of the transmission line is particularly complex considering the 33 individual strands that are twisted together. Hence, to make the modeling easier, an individual strand is initially considered for the purpose of modeling. For an individual strand, the axisymmetric approach of

modeling is adopted initially since the cylindrical geometry of the strand can easily be reproduced by revolving a rectangle around one of its longer axes. The rectangle has dimensions of 2.225mm by 100mm where the axis of revolution coincides with the longer side. The loading too is applied on the entire circular face of the cylinder. This makes the problem completely axisymmetric where both the load and the geometry

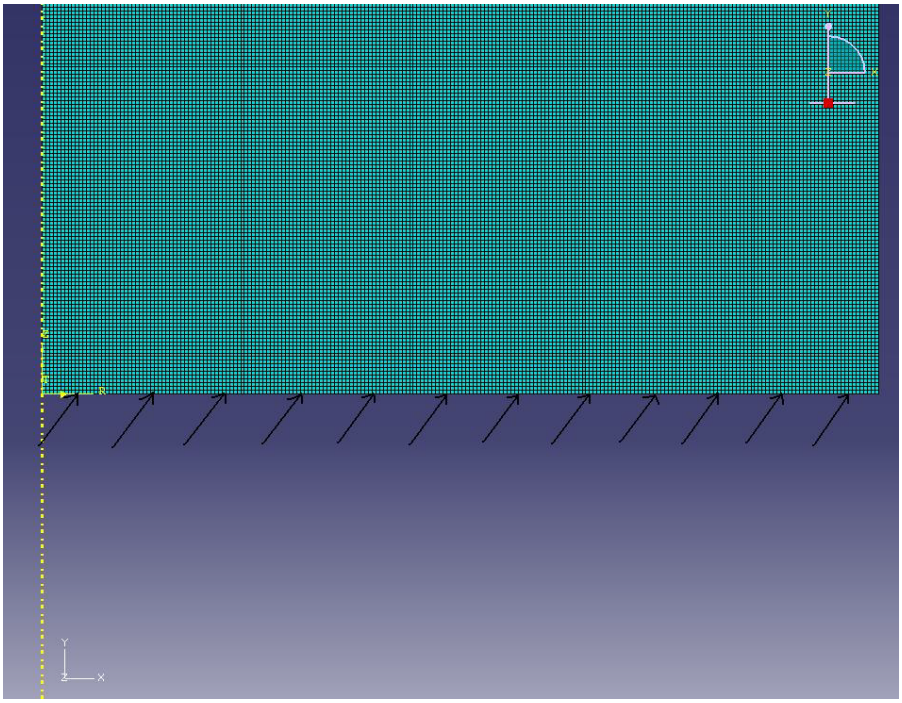

Figure 4.2: Axisymmetric mesh 0.02mm in element size with inclined loads.

are axisymmetric. The loading is applied along the shorter side of the rectangle while the output is recorded at the opposite side. The details are as shown in Figure 4.2.

The second stage of modeling the single strand is the 3D modeling. Here the procedure for modeling is slightly different than the axisymmetric case. Abaqus provides a tool to extrude a 2D figure into a 3D model. Hence, to make a model of a cylinder, it just involves creating a circle of the desired dimension and extruding it through the desired length, which in this case is 100mm. The loading is applied on the one circular face of the cylinder while the output is recorded at the opposite. The Figure 4.3 shows the 3D model of a single strand along with the loading.

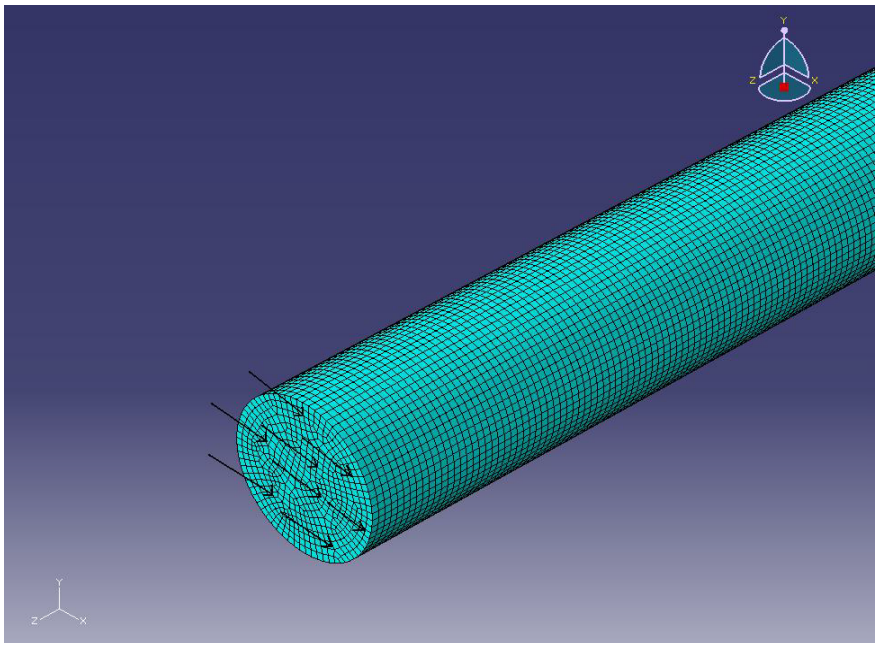

Figure 4.3: 3-D mesh 0.1mm in element size with inclined loads.

The final stage of the modeling is creating the entire 33 strand transmission line in Abaqus. This is one of the most critical tasks of this research and something that makes it unique. The twisting of the alternate strand layers in opposite directions makes this problem even more intricate. The cross-section of the transmission cable is first created in AutoCad, a popular drafting software, and the exact co-ordinates to define the centers of each individual strand are located. The next stage is to create this exact cross-section in Abaqus. Each layer of strands is modeled as a separate part. Hence, in total, there is a single central strand, a layer of 6 strands, another layer of 10 strands and the final layer of 16 strands. Each layer other than the single strand is twisted in the opposite directions. A basic contact condition is defined between the concentric layers. The other important factor of the total model is the fact that the inner 7 strands are of steel having a diameter of 3.5mm while the outer 26 are aluminum having a diameter of 4.45mm. Figure 4.4 shows the FEM model.

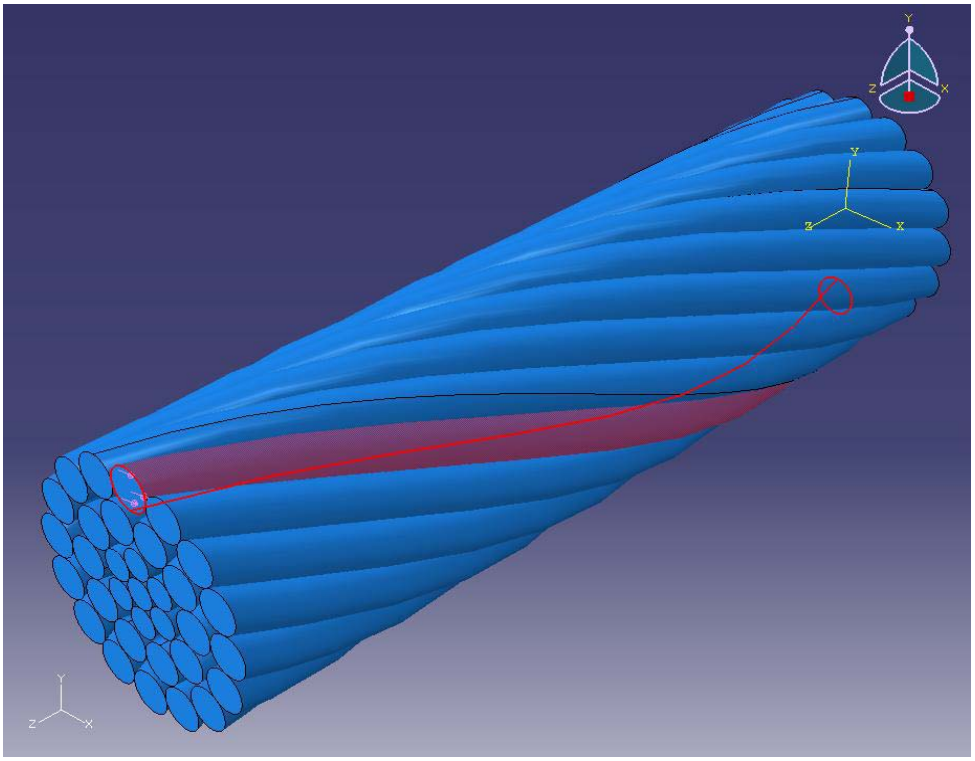

Figure 4.4: 3-D cable with inclined loading on highlighted outer strand.

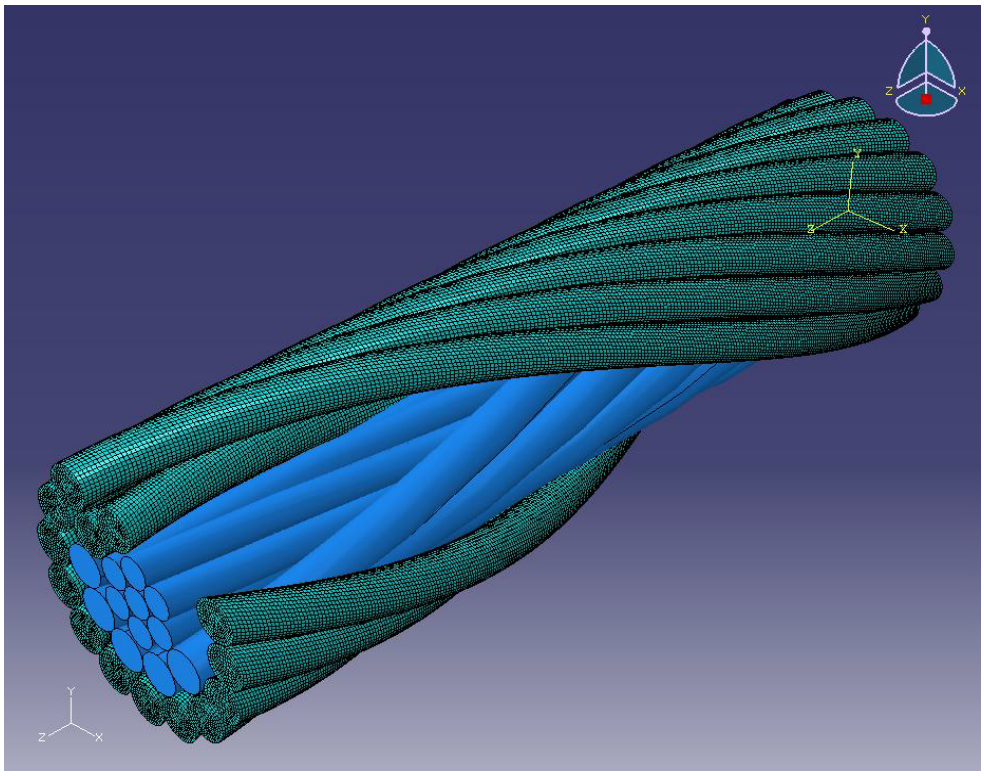

Figure 4.5: 3-D cable model showing opposite twisting layers of strands.

The two materials used for the modeling are steel and aluminum. The steel strands are the load bearing members while the aluminum is used for transmission purposes. The properties for the two materials are as shown in Table 4.1.

Table 4.1: Material properties

Material	Steel	Aluminum
Young's Modulus (GPa)	210	70
Mass Density (Kg/m^3)	7850	2850
Poisson's Ratio	0.30	0.33

4.2 DISCUSSION ON ELEMENTS USED

Choosing an appropriate element is very important in any finite element analysis. Any element is basically characterized by the basic properties of degrees of freedom, number of nodes, formulation and integration. The degrees of freedom are important because they are the fundamental quantities calculated in any analysis. The number of nodes is important because all the unknown quantities are computed at the nodes. In between the nodes these quantities are calculated using the interpolation functions. The order of the interpolation functions depends on the number of nodes.

An element's formulation depends on the mathematical theory used to define the behavior of the element. Depending on the type of problem, this may be Lagrangian or Eulerian. The integration refers to the numerical method that is used to integrate various quantities over the volume of the element. Abaqus uses the Gaussian integration method for most of the problems. If required, elements with reduced integration can also be used. Reduced integration usually means that an integration scheme one order less than the full integration scheme is used. An important point while using elements with reduced integration in computer based finite element software is the fact that they need much less computation time as compared to those with full integration. This factor becomes very important when we have very fine meshes with large number of elements. However a problem associated with the reduced integration is that except in 2D and axisymmetric geometries modeled with higher order elements, the element stiffness matrix becomes rank deficient. This problem is commonly referred to as hourglassing. Since these elements have only 1 integration point (due to reduced integration), it is possible that they

distort in such a way that the strains are zero at that point. In such a case this would give wrong results. Hence, 1st order reduced integration elements are recommended only with very fine meshes. Such problem is not experienced by the 2nd order elements. Since the frequencies to be worked with in this problem are in the ultrasonic range, a fine mesh is desired. Hence, elements with reduced integration are used for both axisymmetric as well as 3D modeling.

For the problem under consideration, its geometry is a three dimensional cylinder. The possible methods for meshing it are using 3D elements like hexahedral, tetrahedral or prism or going for axisymmetric elements. A basic understanding of the finite element method helps in deciding to go with the hexahedral elements for the 3D modeling. Another important aspect requiring mention is that the analysis adopted for this modeling is a dynamic explicit analysis, the reasons for which are explained earlier in this section. One drawback of using this method of analysis is that it does not allow the use of 2nd or higher order elements for meshing. This automatically discards the use of P-type meshing for convergence studies. Hence the research uses the H-type meshing for convergence studies. The C3D8R element is used for the 3D model while the CAX4R element is used for the axisymmetric model. A discussion regarding some fundamental properties of these elements is provided below.

C3D8R:

The notation stands for a 3D continuum 8-node element with reduced integration. It represents a brick element. It is as shown in Figure 4.6.

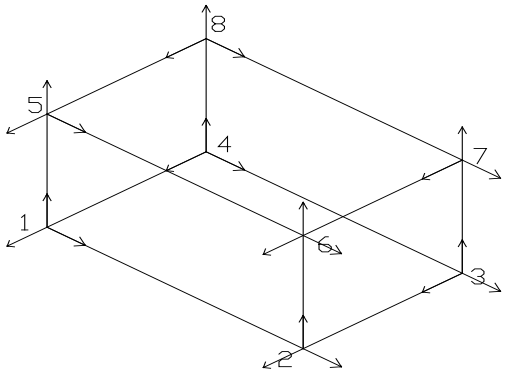

Figure 4.6: 3D continuum 8-node brick element.

As shown in Figure 4.6, it has 8 nodes and hence it is a 1st order element. This makes it a constant strain element. If used in the isoparametric form it can provide more than constant strain response but the higher order terms that the solution contains are not accurate and hence of no use. As discussed in this section, we see that the 2nd order elements are better for meshing but due to the limitation on Abaqus/Explicit we have to use the 1st order brick element. The degrees of freedom active for this element are the displacements in the 3 global axes.

The element uses an isoparametric interpolation. It is defined in terms of the isoparametric coordinates ξ, η, ζ. They have a range of -1 to +1 in each element. The master element with the node numbering is as shown in the Figure 4.7. These are material coordinates since Abaqus is a Lagrangian code.

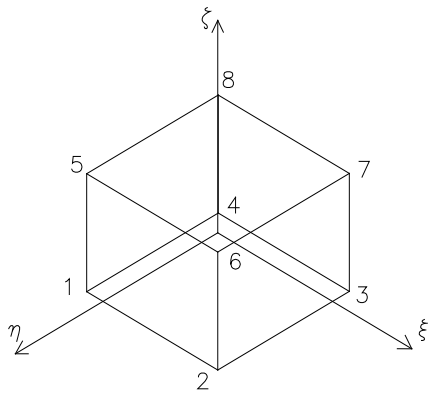

Figure 4.7: Isoparametric brick element.

The interpolation function for the brick element is,

$$u = \frac{1}{8}(1-\xi)(1-\eta)(1-\zeta)u_1 + \frac{1}{8}(1+\xi)(1-\eta)(1-\zeta)u_2$$
$$+ \frac{1}{8}(1+\xi)(1+\eta)(1-\zeta)u_3 + \frac{1}{8}(1-\xi)(1+\eta)(1-\zeta)u_4$$
$$+ \frac{1}{8}(1-\xi)(1-\eta)(1+\zeta)u_5 + \frac{1}{8}(1+\xi)(1-\eta)(1+\zeta)u_6$$
$$+ \frac{1}{8}(1+\xi)(1+\eta)(1+\zeta)u_7 + \frac{1}{8}(1-\xi)(1+\eta)(1+\zeta)u_8. \qquad (4.1)$$

This isoparametric element is integrated using numerical method. Abaqus uses the Gaussian integration method. Since this is a constant strain element, the strain obtained by the Gaussian integration is an averaged value over the entire volume of the element. However the Abaqus/Explicit solver which we use for our analysis uses a different method for calculation of this strain. It is called the *Centroidal Strain Formulation*, which uses the 1 point Gauss integration to obtain the strain at the element center. The purpose

of using this method is to have an improved computational efficiency which again stresses the importance of choosing the correct element and its properties in order to get the best results in an efficient manner.

When we use reduced integration for the 1st order element like C3D8R, hourglassing can make the element unusable. For this Abaqus provides hourglass control in the form of artificial stiffness or artificial damping.

CAX4R:

The notation stands for a 4-node axisymmetric continuum element with reduced integration. The axisymmetric elements use the cylindrical coordinate system given by *r*, *z* and θ. The method involved in producing the cylindrical strand is to create a rectangle (in *r*-*z* plane) with dimensions equal to the radius and length of the strand. This rectangle is then meshed using the CAX4R element. Finally, during analysis, Abaqus revolves the rectangle about its length so as to create the actual geometry. The isoparametric master element for the 4 node element is shown in Figure 4.8.

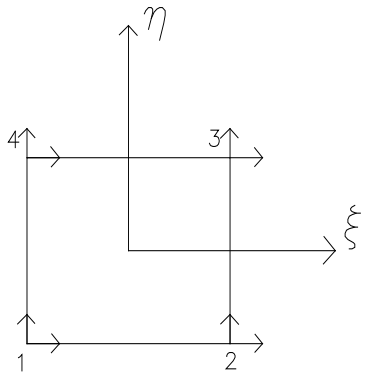

Figure 4.8: Isoparametric 4-node master element.

The active degrees of freedom are the displacements in the *r* and *z* direction. The displacements are the usual isoparametric interpolations with respect to *r* and *z*, augmented by Fourier expansions with respect to θ. The general expression for the interpolation function is as given below

$$u = \sum_{n=1}^{\infty}(u_n \cos n\theta + v_n \sin n\theta), \tag{4.2}$$

where n is the number of terms used in the Fourier interpolation with respect to θ. u_n and v_n are functions of *r* and *z* giving the solution amplitudes.

The integration scheme used for these elements is a product of integration with respect to the element coordinates in surfaces that were originally in the *r*-*z* plane and integration with respect to θ. It is important to control the hourglassing in this element. The hourglassing can vary along the circumference.

5. RESULTS

In Section 2 of this document, the procedure to obtain the analytical or the theoretical dispersion curves was described. The calculation was done in Matlab and the theoretical plots for group velocity versus frequency were obtained. In order to validate the FE model, it is necessary that the group velocity curves obtained by processing data from the FE model should match the theoretical curves. The output from the FE model is in the form of time history for the node velocities in the global X, Y and Z directions.

Using the short-time Fourier Transform (STFT) makes it possible to convert the measured time history signals into time frequency domain. STFT involves analyzing only a small section of a signal at a time. The process is known as signal windowing. The STFT converts a signal into a two-dimensional time-frequency function. The STFT is given by,

$$S\,(\omega, t) = \frac{1}{2\pi} \int_{-\infty}^{\infty} e^{-i\omega\tau} s(\tau) h(\tau - t) d\tau, \tag{5.1}$$

where $h(t)$ is the window function. The window function splits the entire signal into smaller overlapping pieces which are then Fourier transformed individually. The energy density spectrum is called a spectrogram given by

$$E_d \;\; (\omega, t) = |S(\omega, t)|^2. \tag{5.2}$$

Once the time-frequency representations are obtained, it can be easily transformed into the group-velocity-frequency domain by knowing the wave propagation distance *d*.

The relation is given by the simple equation $c_g = d/t$, where c_g is the resulting group velocity and t is the propagation time [14].

As discussed in [14], this procedure is complicated for signals containing reflections and/or discontinuities by the unknown propagation distance d. However, the important feature here is that all signals reflected from any location still propagate within the same model. Hence, all these signals contain a subset of permissible Lamb modes inherent to the model. For known propagation distance, the group-velocity representations will be similar. Due to the reflections a number of changes can take place in the representations. These changes could involve complete disappearance of some modes, new modes being visible or even change in the frequency content of some modes.

This section looks at the results obtained from different simulations. These simulations are varied mostly in the method in which the load was applied. The mesh size is left the same for most of them. The mesh size governs the run-time and memory requirements for the simulations. As explained earlier, this analysis allowed on H-type meshing for convergence studies. Hence the mesh size is progressively reduced in order to study the convergence of the solution. The simulation is started with the axisymmetric model having a mesh size of 0.02mm. This size is chosen considering the recommendations given in [10]. Figure 5.1 gives the time domain signal from which Figure 5.2 was obtained. Figure 5.2 shows the results for this simulation. The velocity time histories obtained from Abaqus are converted into the group-velocity-frequency representation as explained before. The output is then superimposed with the theoretical group velocity dispersion curves.

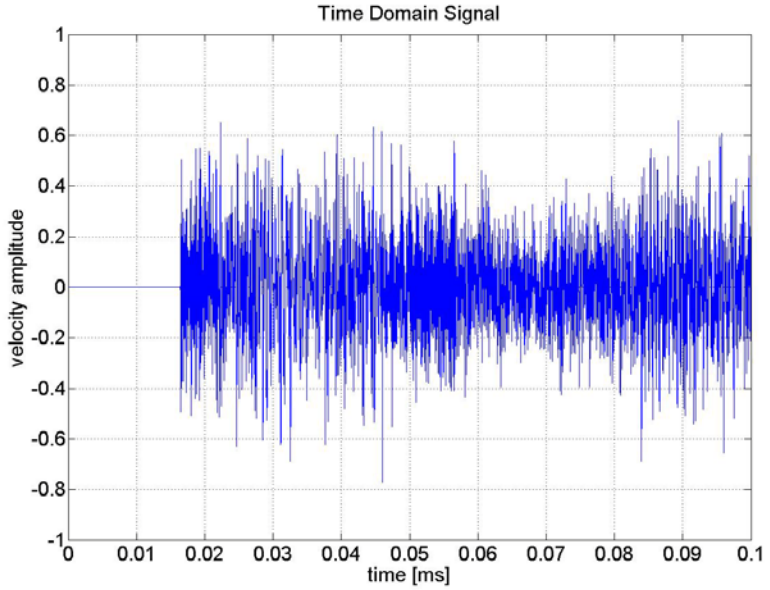

Figure 5.1: Time domain signal for axisymmetric single strand model of mesh size of 0.02mm subject to a pulse of 10 MHz.

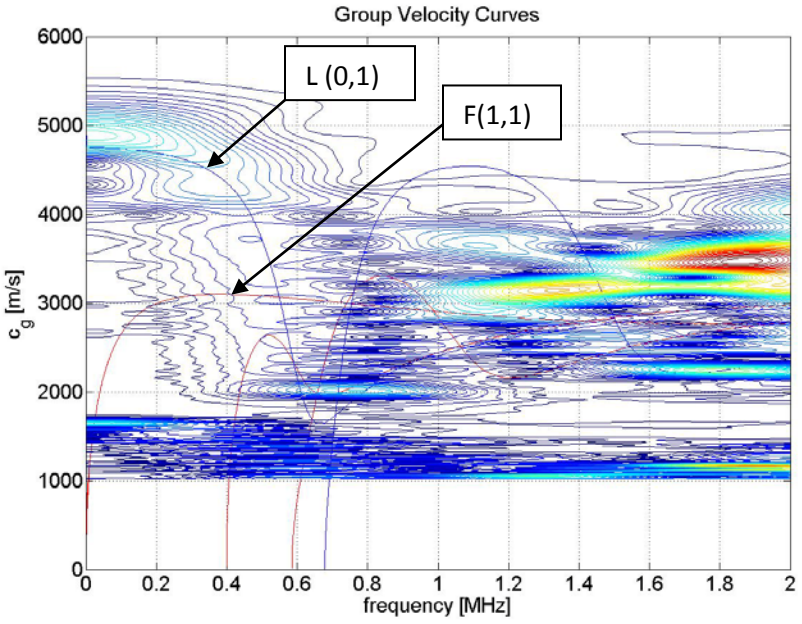

Figure 5.2: Group velocity curve for axisymmetric single strand model of mesh size of 0.02mm subject to a pulse of 10 MHz.

Figure 5.2 shows that the first longitudinal mode from the FE analysis seems to be matching well with the theoretical curve. But anything beyond that doesn't seem to match with any of the theoretical curves. The runtime for this simulation is around 6 hours on the supercomputer Hydra (IBM p5-575 Cluster 1600) provided by Texas A&M Supercomputing.

Since Figure 5.2 showed only the 1st longitudinal mode L(0,1), the mesh is tested for being coarse, thus not giving the correct results. Making the mesh finer is an option but it comes at the cost of increasing the runtime and memory requirements. Hence, instead of 10 MHz, a pulse of 1 MHz is used. Figure 5.3 gives the time domain signal while Figure 5.4 shows the results for this simulation.

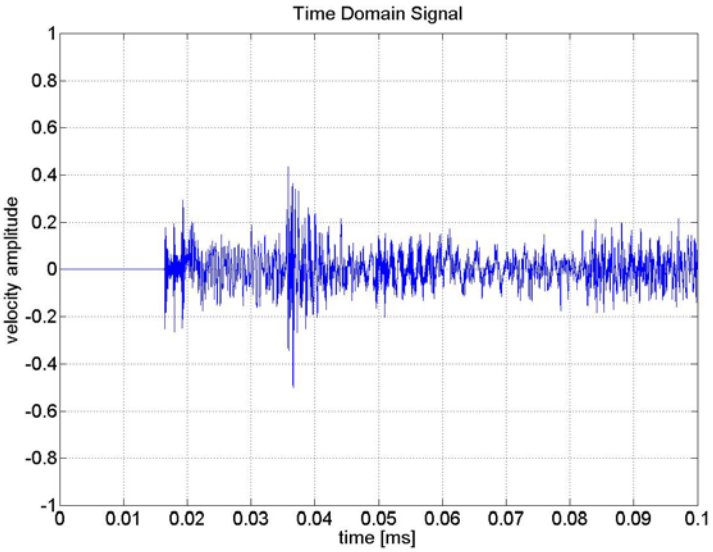

Figure 5.3: Time domain signal for axisymmetric single strand model with mesh size of 0.02mm subject to a pulse of 1MHz.

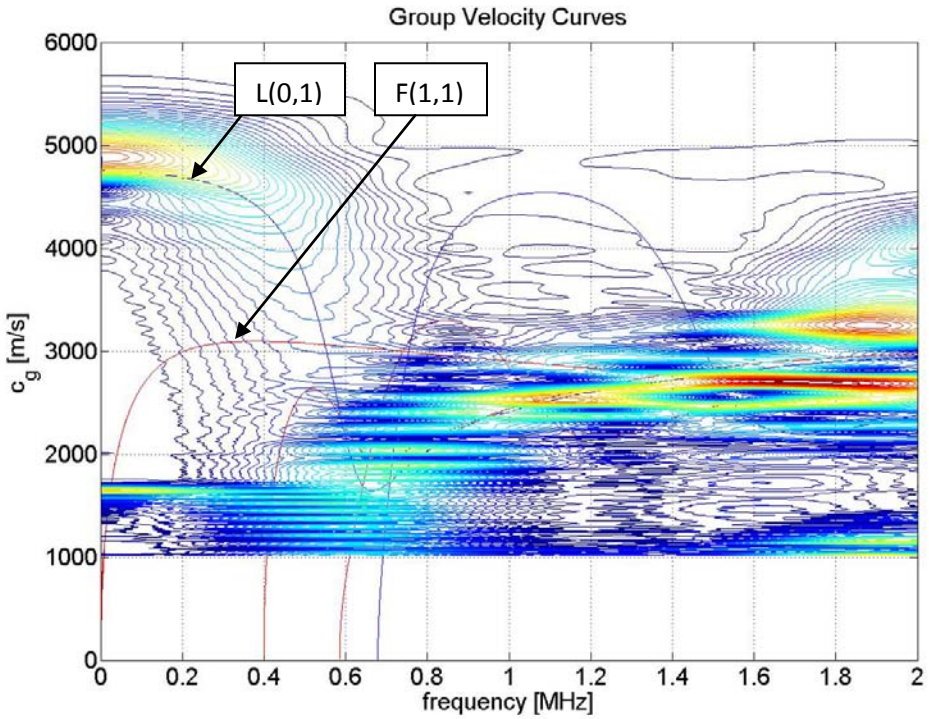

Figure 5.4: Group velocity curve for axisymmetric single strand model with mesh size of 0.02mm subject to a pulse of 1MHz.

.

Figure 5.4 clearly shows that the 1st longitudinal mode. If one compares Figures 5.2 and 5.4, one can see that the L(0,1) mode has significantly improved and now matches much better with the theoretical mode. But once again, L(0,1) is the only mode visible in the FE analysis representation. There are some traces of a mode from 1 MHz to 2 MHz and between the group velocities of 2000 m/s and 3000 m/s. This is the Rayleigh wave velocity mode. It is the mode to which all other modes would eventually converge.

A number of attempts are made to get the other dispersion curves as well. Figure 5.5 shows the time domain signal for a simulation that has the same configuration as

Figure 5.4, the only difference being the load applied as traction instead of pressure. Figure 5.6 gives the results for the same.

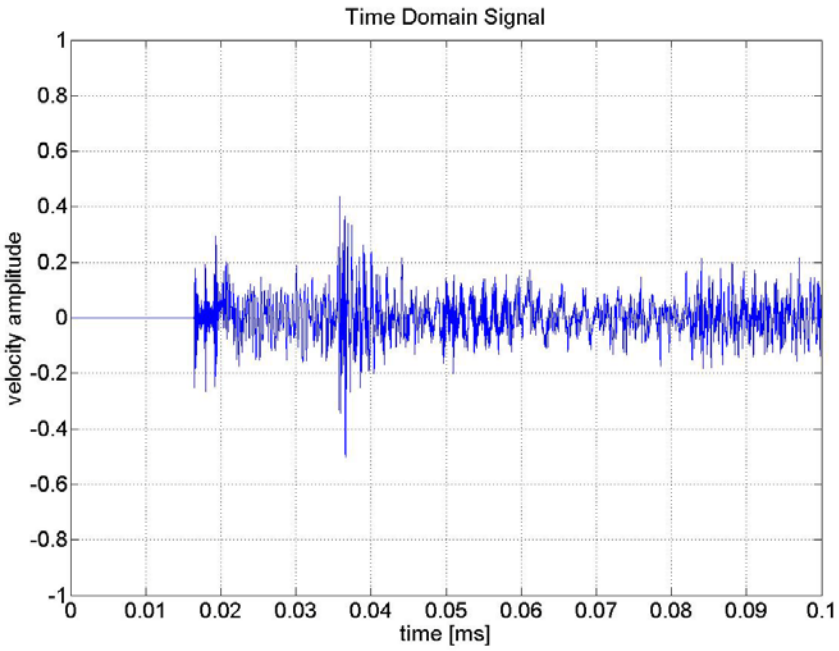

Figure 5.5: Time domain signal for axisymmetric single strand model with mesh size of 0.02mm subject to a pulse of 1MHz applied as traction.

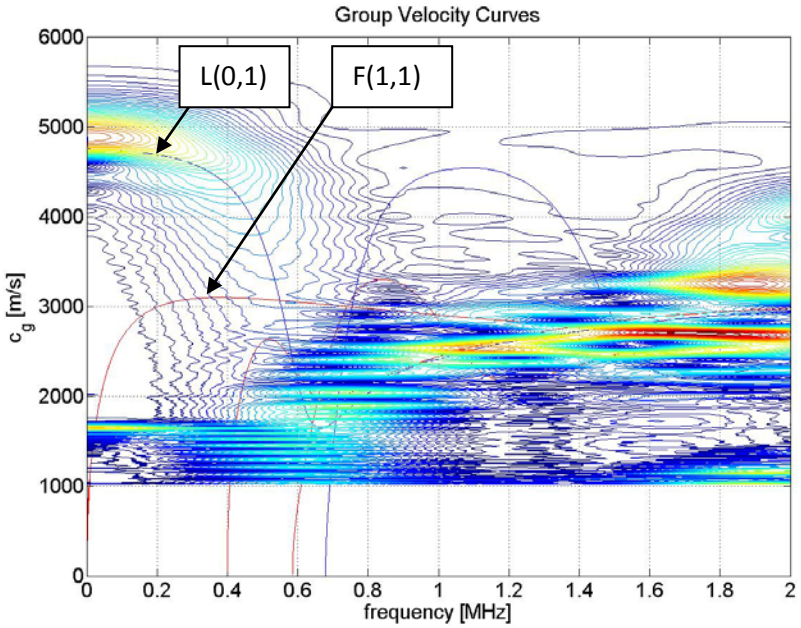

Figure 5.6: Group velocity curve for axisymmetric single strand model with mesh size of 0.02mm subject to a pulse of 1MHz applied as traction.

Figure 5.6 also shows a lot of similarity to Figure 5.4. Both figures show the L(0,1) mode quite well and also give some indications of the Rayleigh wave velocity mode, but there are no signs of any of the flexural modes. A possible cause for this could be the loading direction. Initially the loading is applied in the longitudinal or transverse direction to the axisymmetric model. Another simulation is attempted by applying the loading in the inclined direction. It is assumed that the inclined loading would induce both the longitudinal as well as the flexural modes in the model. The time domain signals are given by figure 5.7 while the results for the same are shown in Figure 5.8

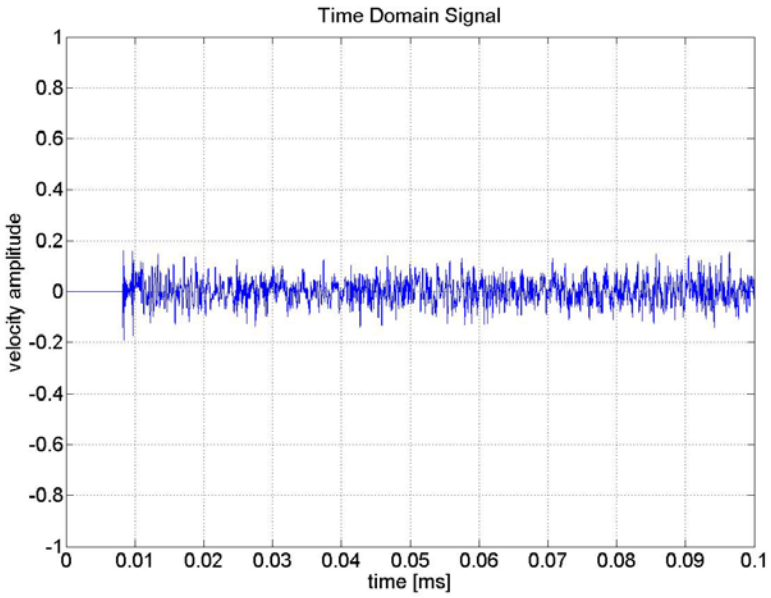

Figure 5.7: Time domain signal for axisymmetric single strand model with mesh size of 0.02mm subject to a pulse of 1MHz applied in the inclined (45^{o}) direction.

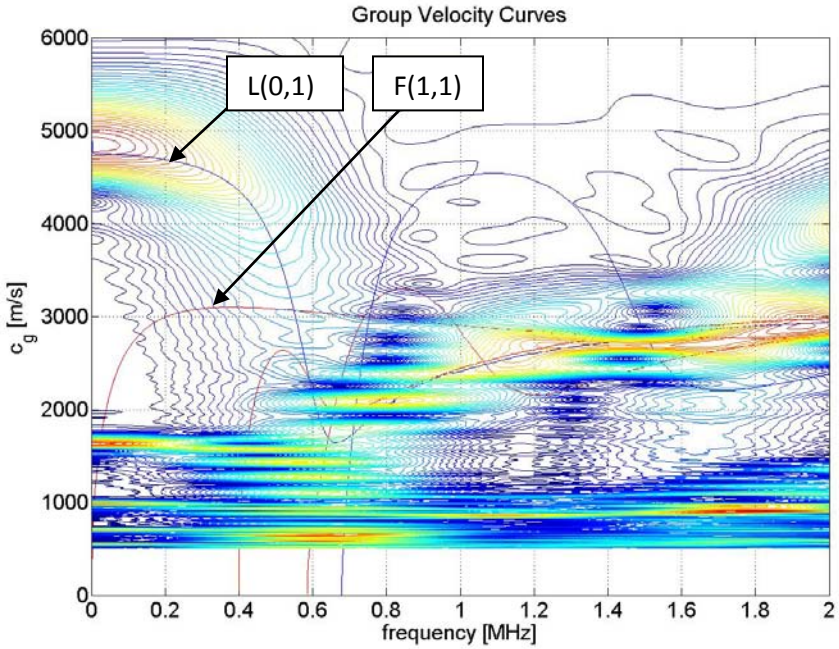

Figure 5.8: Group velocity curve for axisymmetric single strand model with mesh size of 0.02mm subject to a pulse of 1MHz applied in the inclined (45^{o}) direction.

Some other trials mostly involve changing the type and direction of loading or changing the pulse width and accordingly the mesh size. The output is recorded at different nodes so as to try and get both the symmetric as well as the anti-symmetric modes. However, in each of these trials the same results are obtained with the L(0,1) mode being the dominant one and some indications of the Rayleigh wave velocity mode. As a last attempt for the axisymmetric model, it is decided to use a very fine mesh. Abaqus has a smallest element size limitation of 0.004mm. This mesh is used for the axisymmetric model. To reduce the overall size of the model, the length is reduced to 50mm. Inspite of reducing the model length; it contains a staggering 4.45 million elements within an area of 2.225mm by 50mm. There are a total of 4460446 nodes and 8920892 variables to compute. This problem would require a large amount of computing power and time. The supercomputing department at Texas A&M helped this requirement by authorizing the use of a special queue without pre-emption for this particular simulation. Protection against pre-emption assures the continuous running of the simulation as well. The output is requested at a select few nodes only so as to make it easy for the solver to write the output to the output database file and also to reduce the overall size of the database. The simulation runs for a total time of about 129 hours or 5 full days and 9 hours. The time domain signal is given by Figure 5.9 while the processed output is as shown in Figure 5.10. Once again we see that the 1st longitudinal mode L(0,1) is present along with indications of the Rayleigh wave velocity mode.

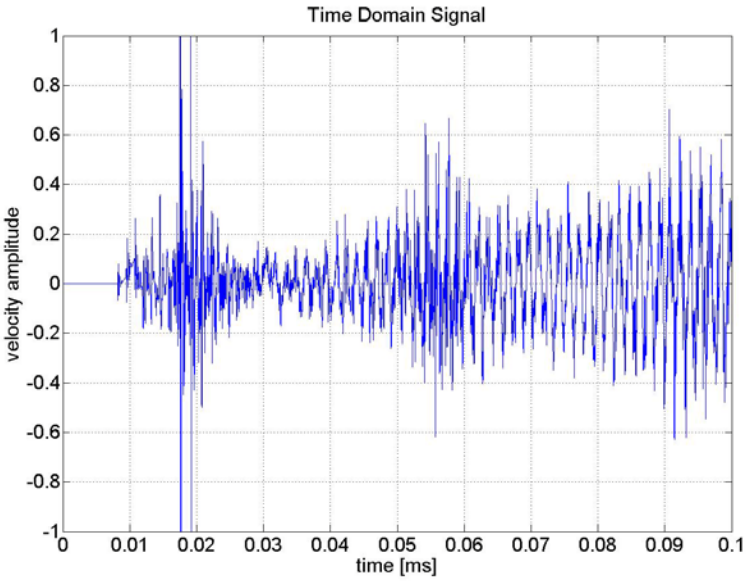

Figure 5.9: Time domain signal for axisymmetric single strand model with mesh size of 0.004mm subject to a pulse of 1MHz applied in inclined (45^{o}) direction.

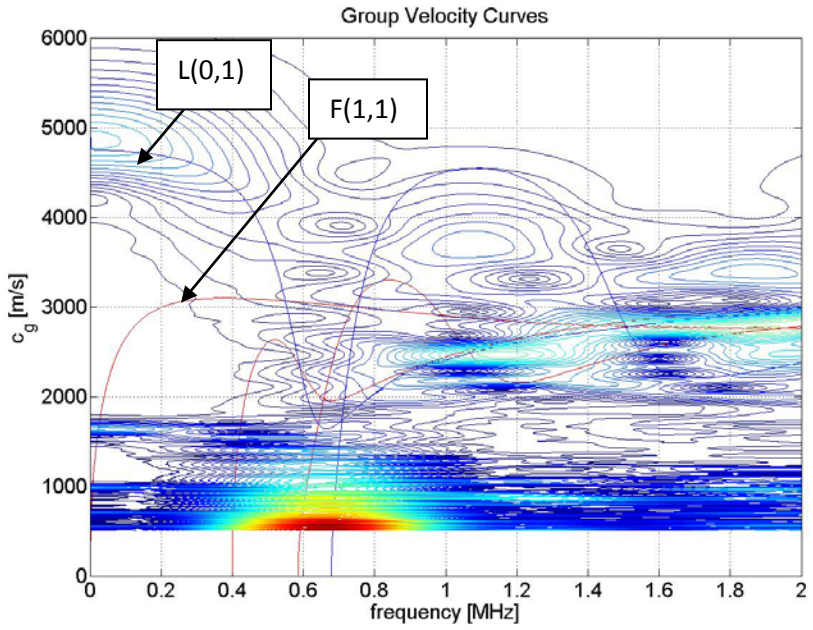

Figure 5.10: Group velocity curve for axisymmetric single strand model with mesh size of 0.004mm subject to a pulse of 1MHz applied in inclined (45^{o}) direction.

The next step in the research is using a 3-D model instead of the axisymmetric one and run similar set of simulations. The 3-D model should give better results compared to the axisymmetric model. However, the 3-D model would require more time and memory compared to the axisymmetric model for the same mesh density. Figure 5.11 gives the time domain signal and Figure 5.12 shows the group velocity dispersion curves for a 3-D model subjected to a 1 MHz pulse as load with an element size of 0.1mm. Looking at the results for the axisymmetric case, the load is applied in the inclined (45^o) direction in the form of traction. We see that neither modes are visible in the figure.

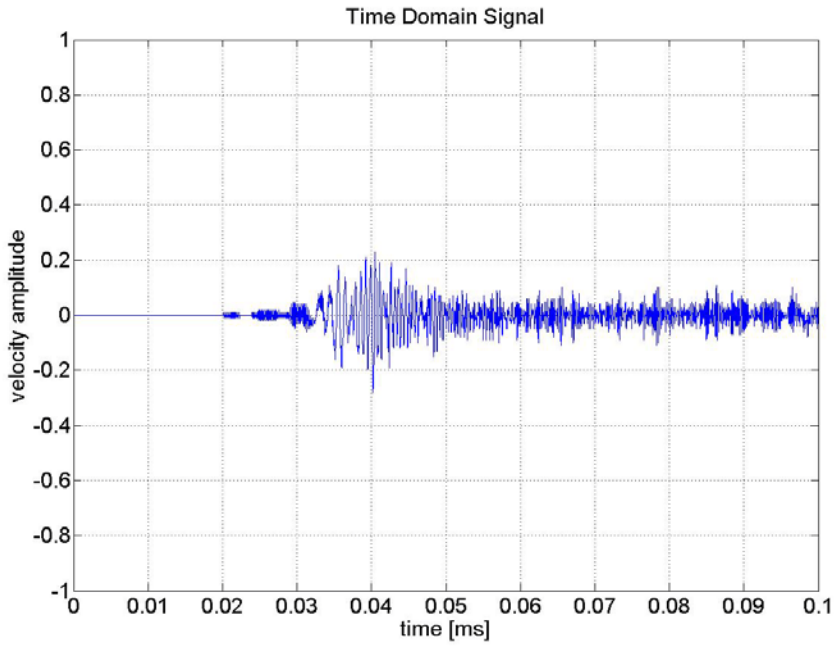

Figure 5.11: Time domain signal for 3-D single strand model with mesh size of 0.1mm subject to a pulse of 1MHz applied in inclined (45^o) direction.

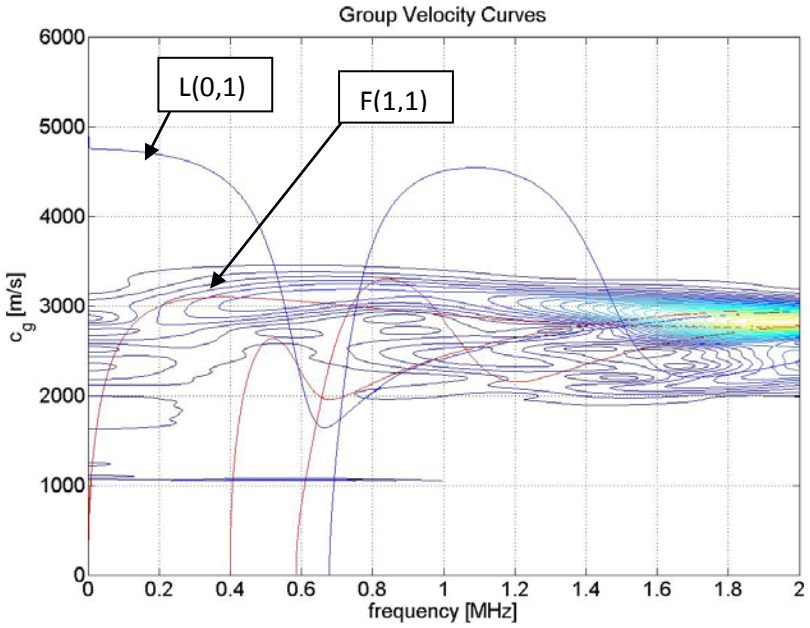

Figure 5.12: Group velocity curve for 3-D single strand model with mesh size of 0.1mm subject to a pulse of 1MHz applied in inclined (45^{o}) direction.

The next simulation that is tried involves the loading being applied in the longitudinal direction in the form of traction again. The results are shown in Figure 5.12 and Figure 5.14. We see that there is not much change as far as depicting the group velocity modes is concerned between Figure 5.12 and 5.14. The next figures show the results for the simulation which has loading along the longitudinal direction in the form of pressure and not traction. Figure 5.15 shows the time domain and Figure 5.16 shows the velocity curves recorded along the longitudinal direction while Figure 5.17 and Figure 5.18 respectively show the same but recorded in the transverse direction.

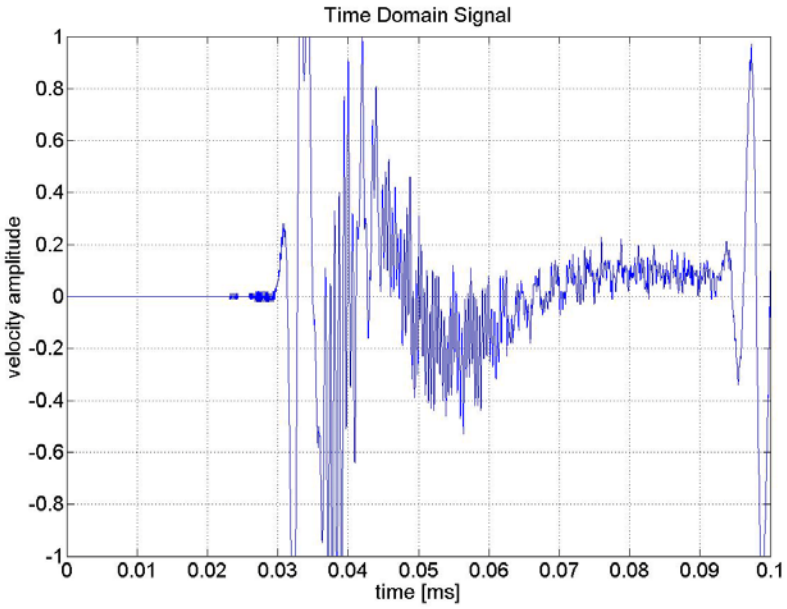

Figure 5.13: Time domain signal for 3-D single strand model with mesh size of 0.1mm subject to a pulse of 1MHz applied in longitudinal direction.

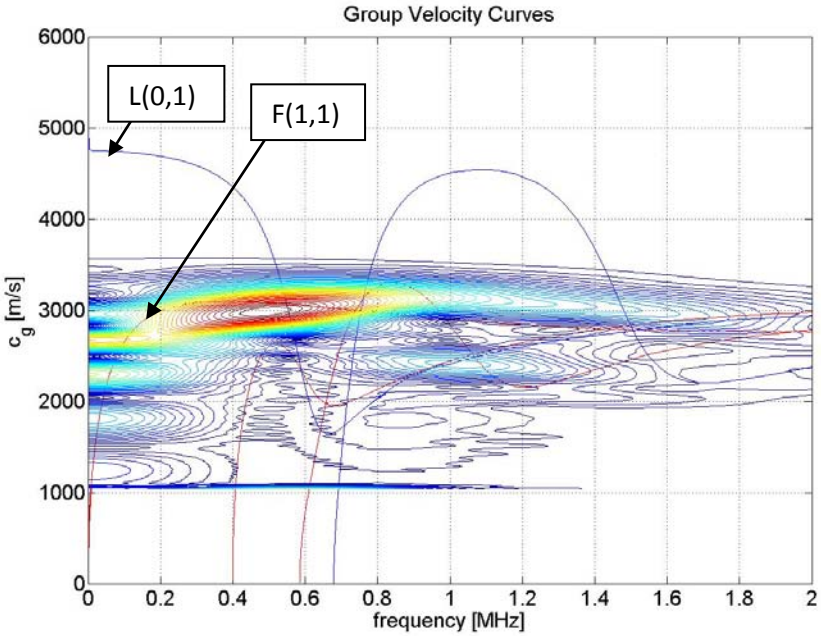

Figure 5.14: Group velocity curve for 3-D single strand model with mesh size of 0.1mm subject to a pulse of 1MHz applied in longitudinal direction.

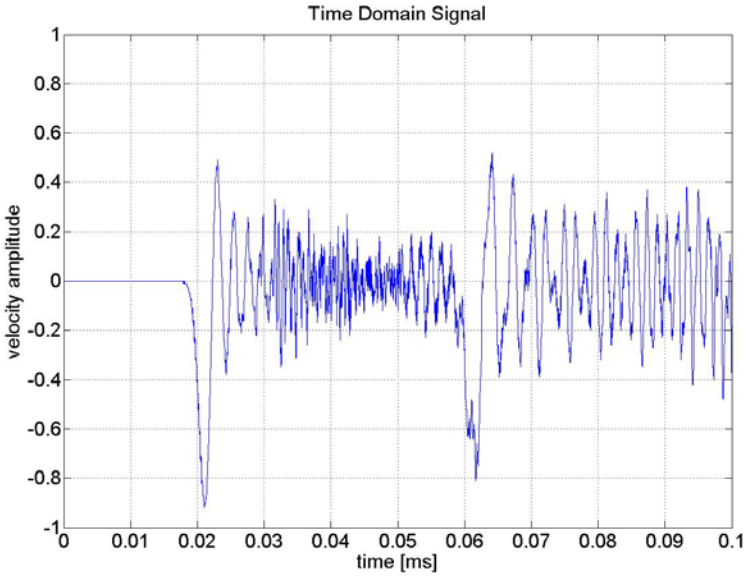

Figure 5.15: Time domain signal for 3-D single strand model with mesh size of 0.1mm subject to a pulse of 1MHz applied as pressure in longitudinal direction.

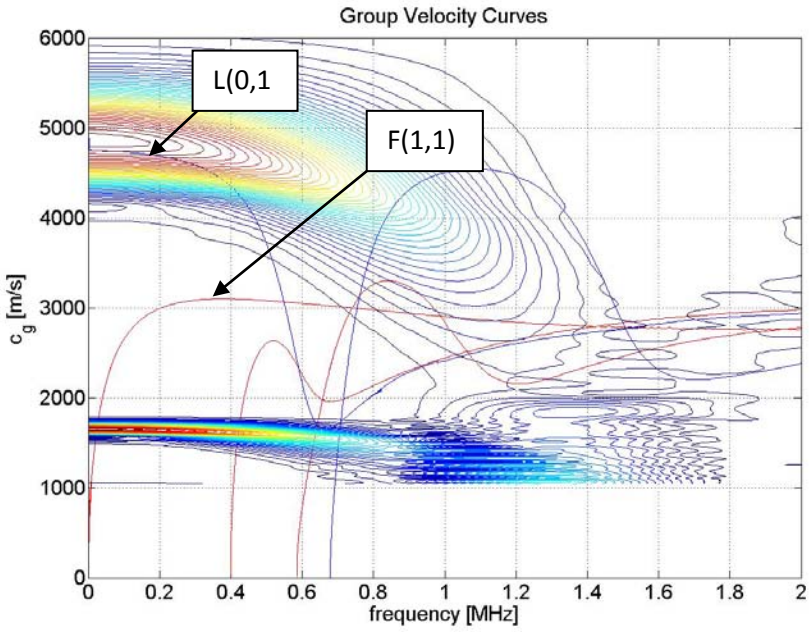

Figure 5.16: Group velocity curve for 3-D single strand model with mesh size of 0.1mm subject to a pulse of 1MHz applied as pressure in longitudinal direction.

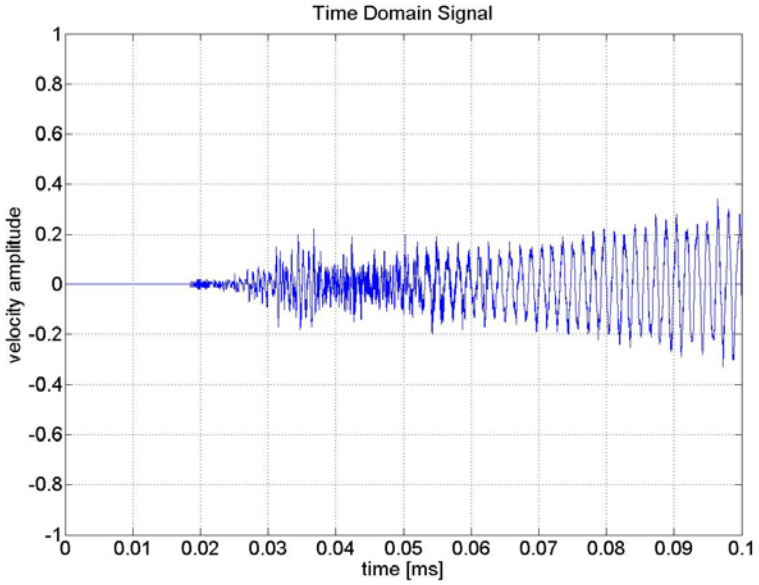

Figure 5.17: Time domain signal for 3-D single strand model with mesh size of 0.1mm subject to a pulse of 1MHz applied as pressure in transverse direction.

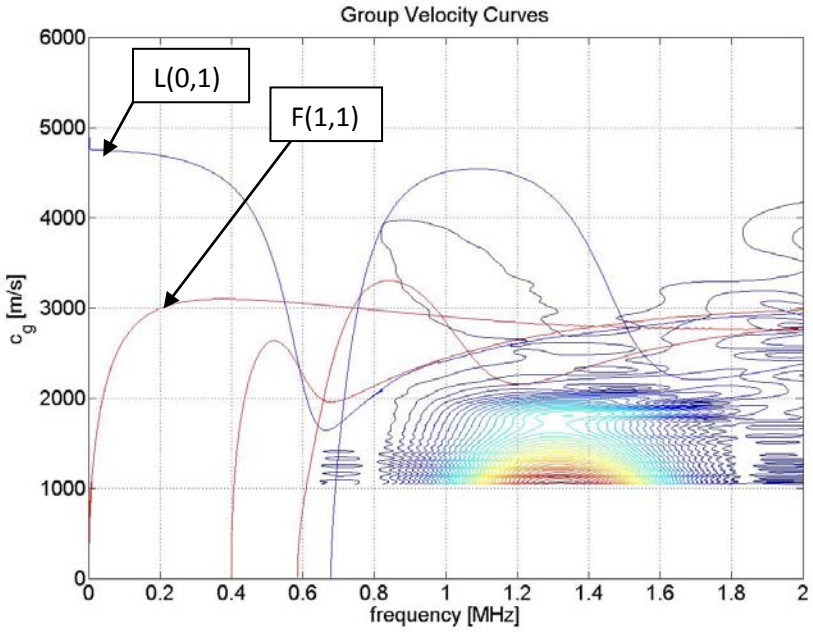

Figure 5.18: Group velocity curve for 3-D single strand model with mesh size of 0.1mm subject to a pulse of 1MHz applied as pressure in transverse direction.

In all these figures we see that none of them depict any of the velocity modes in an acceptable manner. Figure 5.16 is the one which comes closest in giving the 1st longitudinal mode L(0,1). However, even that is not accurate. The 3-D model uses the C3D8R element through these models. The reduced integration (denoted by R in the element name) could be responsible for suppressing the modes since it introduces artificial damping as explained in earlier sections. Hence, another simulation is performed which contained the element C3D8, a simple 8-noded hexahedral element without reduced integration. The loading used was again a 1 MHz pulse applied in the inclined direction (45^{o}) as traction. Figure 5.19 shows the time domain signal and Figure 5.20 shows the processed results.

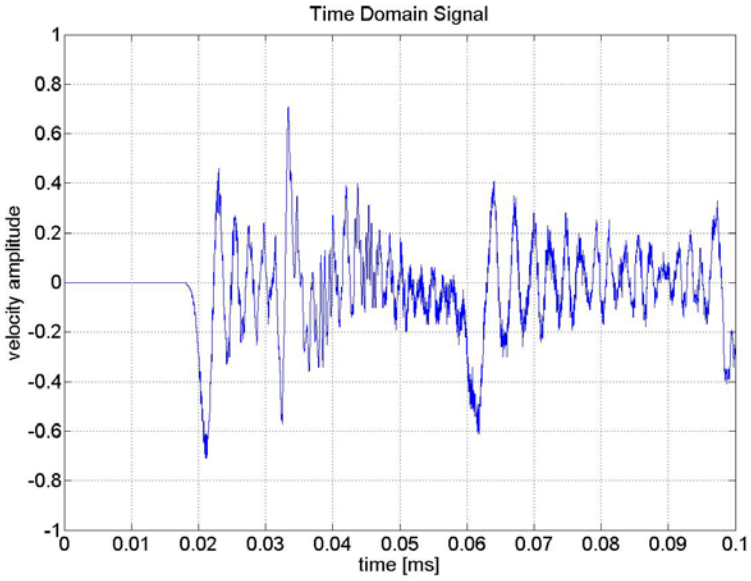

Figure 5.19: Time domain signal for 3-D single strand model with mesh size of 0.1mm subject to a pulse of 1MHz applied as traction in the inclined direction.

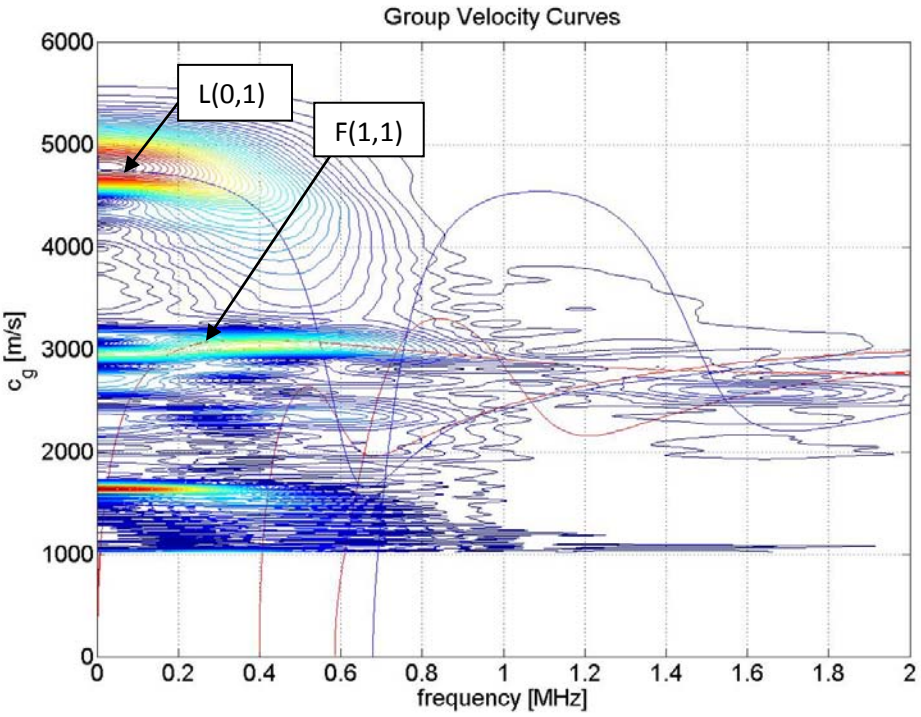

Figure 5.20: Group velocity curve for 3-D single strand model with mesh size of 0.1mm subject to a pulse of 1MHz applied as traction in the inclined direction.

However any more simulations using the C3D8 element does not provide any better results than what is already available. Also, comparing the results between the axisymmetric and the 3-D single strand models, it can be concluded that load applied as traction in the inclined direction was more or less giving the 1st longitudinal mode in both the models. Hence the same method for loading is decided to be used for the 3-D model of the entire cable. The mesh size for the cable model is only 0.4mm. The reason for that is the memory limitation of the computer. Any chance to make the mesh finer terminates Abaqus citing memory limit exhaustion. Figure 5.21 gives the time domain results Figure

5.22 gives the group velocity results for the total cable model. Here the loading is applied to an external strand and recorded at the end of the same strand.

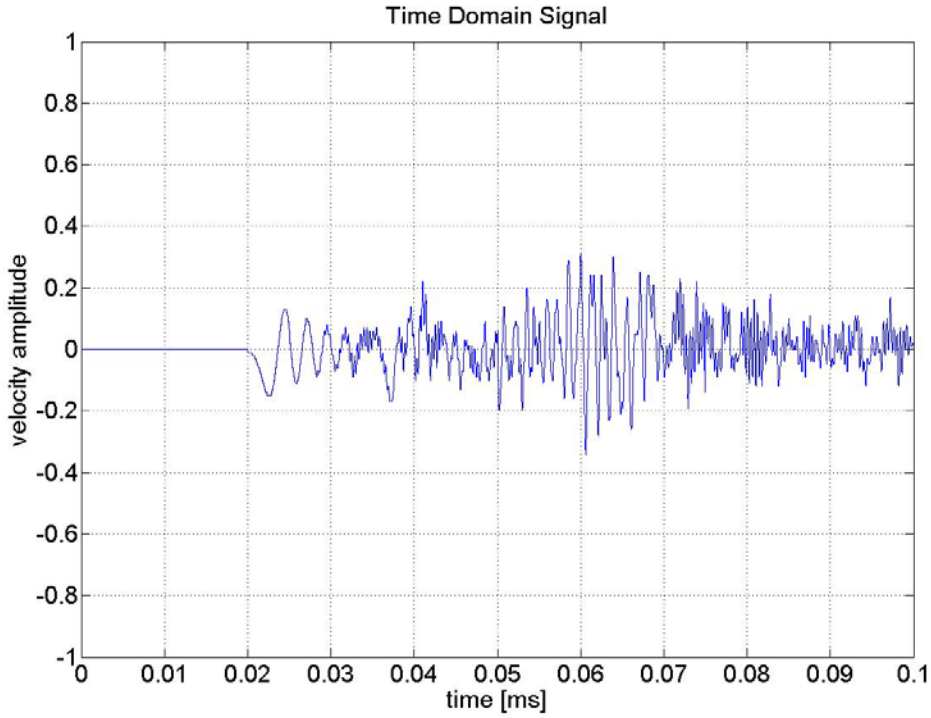

Figure 5.21: Time domain signal for 3-D cable model with mesh size of 0.4mm subject to a pulse of 1MHz applied as traction in the inclined direction.

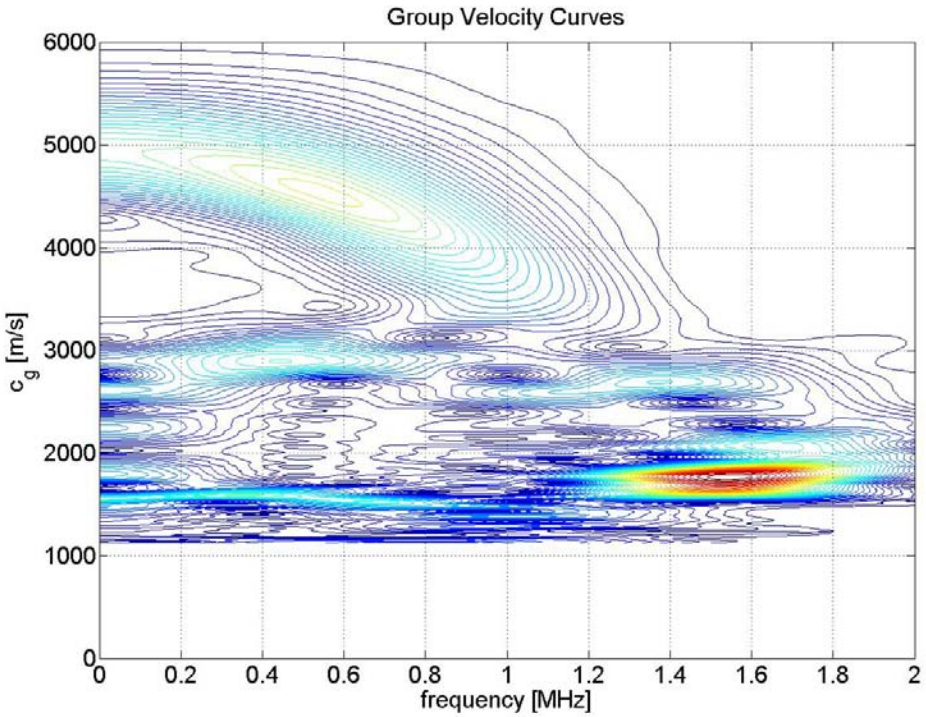

Figure 5.22: Group velocity curve for 3-D cable model with mesh size of 0.4mm subject to a pulse of 1MHz applied as traction in the inclined direction.

Initial observation of the Figure 5.22 indicates some hints of a mode similar to the 1st longitudinal mode in the single strand.

The next task is to introduce a cut in one of the strands of the model and observe the change in the output. Figure 5.23 gives the corresponding time domain signal in which one can clearly see the two peaks. The first one is corresponding to the load application while the second is for the wave reflection after it has covered a total distance of 200mm. The time interval between the two peaks matches with the distance the wave has to cover and the expected bulk velocity of the wave. Figure 5.24 gives the group

velocity curves for an undamaged model in which the axial particle velocity is recorded at the location of application of the pulse.

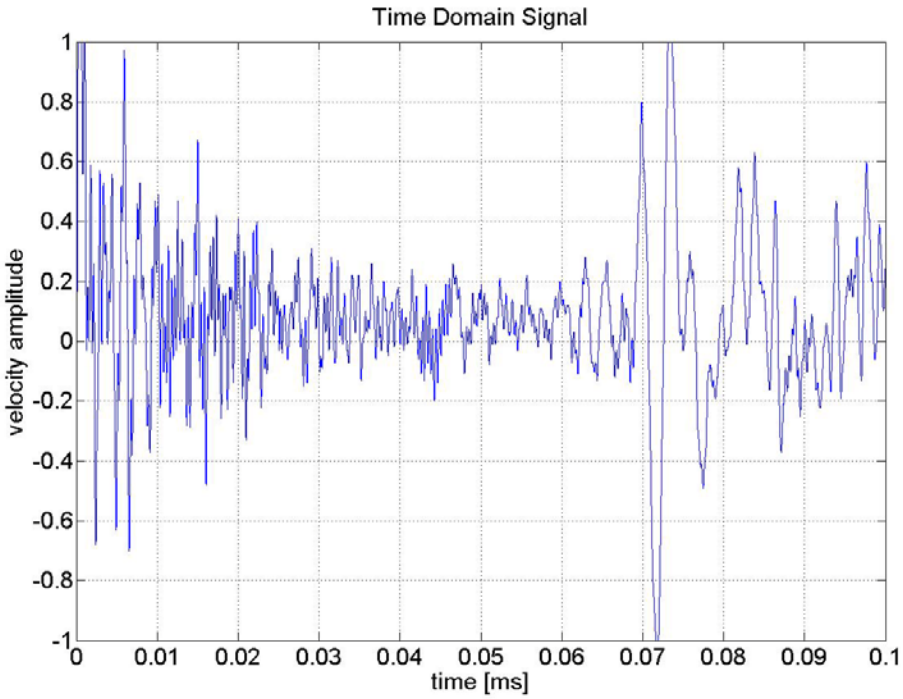

Figure 5.23: Time domain signal for an undamaged 3-D cable model with mesh size of 0.4mm subject to a pulse of 1MHz applied as traction in the inclined direction.

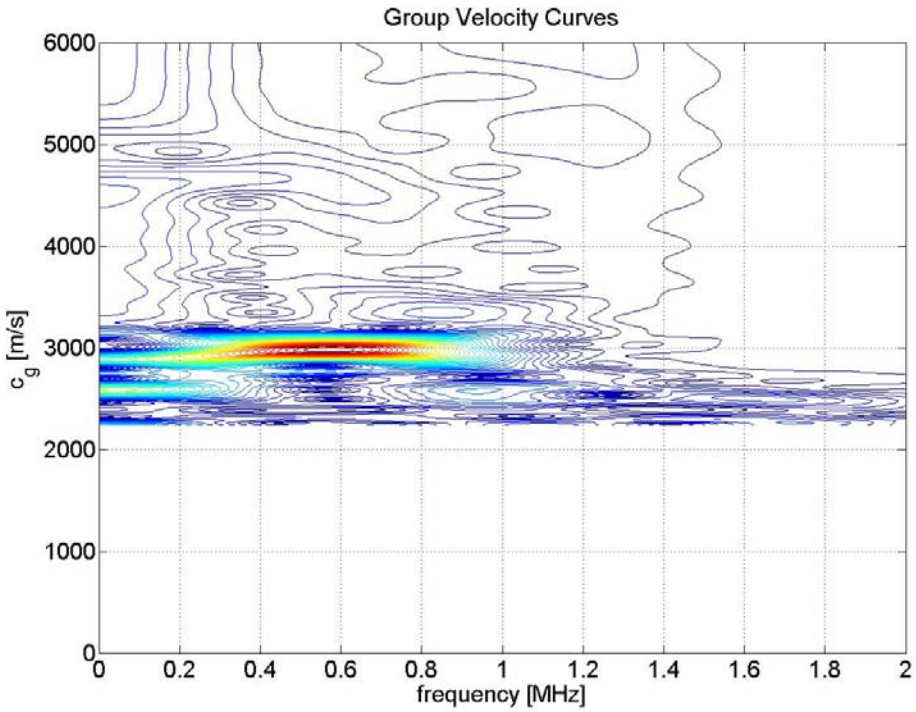

Figure 5.24: Group velocity curve for an undamaged 3-D cable model with mesh size of 0.4mm subject to a pulse of 1MHz applied as traction in the inclined direction.

The damage is induced at middle of the strand (50mm) in the form of a complete crack. Figure 5.25 gives the time domain signal recorded for this simulation. Since in this case, the pulse has to cover only a distance of 100mm, we can see exactly twice the number of peaks in the time domain signal as compared to that of the undamaged model. Figure 5.26 gives the group velocity curves for a damaged model in which the axial particle velocity is recorded at the location of the load application.

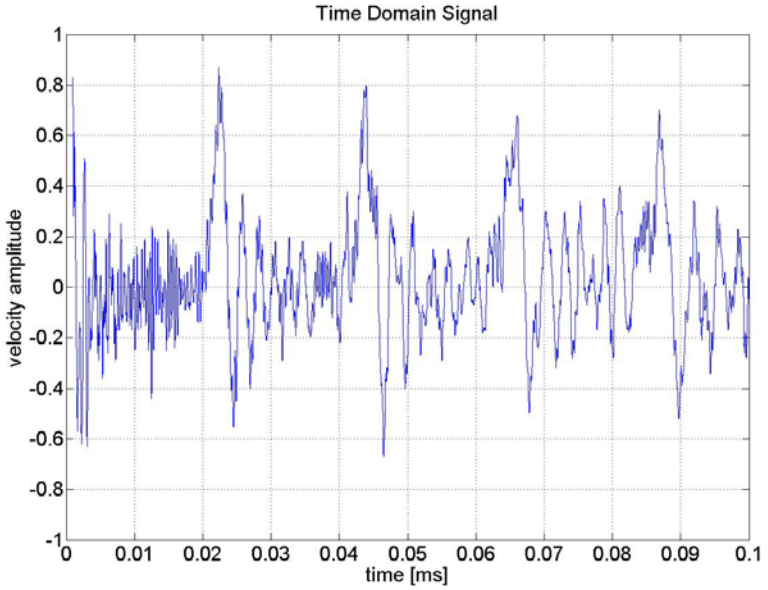

Figure 5.25: Time domain signal for a damaged 3-D cable model with mesh size of 0.4mm subject to a pulse of 1MHz applied as traction in the inclined direction.

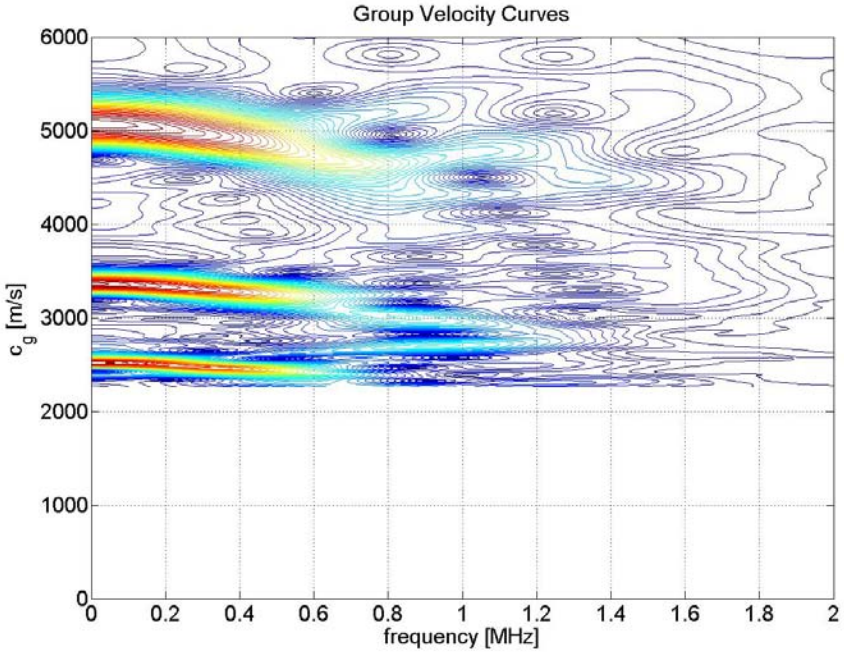

Figure 5.26: Group velocity curve for a damaged 3-D cable model with mesh size of 0.4mm subject to a pulse of 1MHz applied as traction in the inclined direction.

6. CONCLUSIONS AND FUTURE RESEARCH

The conclusions of this research can be broadly classified into two types. First would be the experimental conclusions while second would be those based on the finite element study. In this research, the feasibility of continuous, on-line monitoring of power lines using ultrasonic waves is considered. First a brief review in the theory of guided waves of rods is presented. It turns out that wave propagation in a single strand is complicated due to the multi-mode and dispersive nature of the guided wave and is even more complicated for a transmission line consisting of twisted strands of two different materials. The result of the attenuation coefficient of the transmission line is that a guided wave can propagate over a very long distance, so it will be possible to have a limited amount of sending/receiving transducers to monitor the power line.

Finally, the experimental study shows that the damage in a transmission line can be detected. A defect in the cable will cause a portion of the incident ultrasonic wave to be reflected back to the transducer. It is also obvious that when a piezoelectric ring-actuator is used for the excitation of the ultrasound, the ultrasound is better coupled in to the outer strands than to the inner strands. However, it is shown that ultrasonic waves do indeed propagate in the inner strands.

Section 5 shows the results obtained from the finite element simulations. One common result clearly seen in all the single strand simulation results is the 1st longitudinal mode L(0,1). For both the axisymmetric as well as the 3-D single strand models, the 1st longitudinal mode can be seen quite well. The only other mode visible is

the Rayleigh wave velocity mode to which all the longitudinal and the flexural modes would eventually coincide. The amount of simulations tried to obtain the remaining modes suggests the need for a different approach to model the strands as well as complete cable. Also, more research is needed to make the simulations economically viable as far as run-time and memory requirements are considered.

The future research would involve getting all the dispersion modes from the finite element model. The next major step would then be to introduce a crack in the strands and then study the change in behavior of the dispersion curves. Once obtained, the proposed methodology can be used for continuous monitoring of the transmission line. The technology can also be used to monitor other cable structures such as suspension or cable-stayed bridges.

REFERENCES

[1] U.S. Helicopter summary statistics: Helicopter Association International 1997-2006 Website: www.rotor.com/Default.aspx?tabid=597

[2] Meitzler, A, Mode coupling occurring in the propagation of elastic pulses in wires. Journal of Acoustical Society of America 1961; 33, 4:435-445

[3] Rizzo, P, Lanza di Scalea, F. Monitoring steel strands via ultrasonic measurements. In: Proceedings of SPIE 2002 - The International Society for Optical Engineering; Seattle, Washington; 4696:62-73.

[4] Rizzo, P, Lanza di Scalea, F. Wave propagation in multi-wire strands by wavelet-based laser ultrasound. Experimental Mechanics 2004; 44, (4):407-415.

[5] Rizzo, P, Lanza di Scalea, F. Ultrasonic inspection of multi-wire steel strands with the aid of the wavelet transform. Journal of Smart Materials and Structures 2005; 14:685-695.

[6] Washer, G A, Green, R E, Pond, R B. Velocity constants for ultrasonic stress measurement in pre-stressing tendons. Journal of Research in Nondestructive Evaluation 2002; 14:81-94.

[7] Jayasinghe, J A S B, Aggarwal, R K, Johns, A T, Downes, J. New approach to condition monitoring of high voltage overhead lines using neural networks. In: Proceedings of the 1999 11th International Symposium on 'High Voltage Engineering', IEE Conference Publication, London, United Kingdom, 1, 467:1.33-S3-1.36.S3.

[8] Aggarwal, R K, Johns, A T, Jayasinghe, J A S B, Gwyn, B, Stone, R, Cameron, C. Simulation of the partial discharge phenomena in defective overhead line conductors through an empirical approach. In: Proceedings of the 1998 International Conference on Simulation, IEE Conference Publication, York, United Kingdom, 457:385-389.

[9] Muraoka, M, Mitani, I, Inagaki, J. Microprocessor-based fault locator. Toshiba Review (International Edition), 1984; 148:11-14.

[10] Moser, F, Jacobs, L, J, Qu, J. Modeling elastic propagation in waveguides with the finite element method. NDT&E International 1999; 32:225-234.

[11] Protopappas, V. Three-dimensional finite element modeling of guided ultrasound wave propagation in intact and healing long bones. Journal of Acoustic Society of America 2007; 121(6):3907-3921.

[12] Graff, K.F. Wave motion in solids. New York: Dover Publications Inc; 1999.

[13] Hurlebaus, S. Smart structures: Fundamentals and applications. Lecture Notes. Zachry Department of Civil Engineering, Texas A&M University; 2005.

[14] ABAQUS version 6.7, ABAQUS Analysis user's manual. Hibbitt, Karlsson and Sorensen Inc., 2007, Pawtucket, Rhode Island.

[15] Hurlebaus, S. A contribution to structural health monitoring using elastic waves, 2002, Doctoral Thesis, University of Stuttgart.

SUPPLEMENTARY REFERENCES

ABAQUS version 6.7, ABAQUS theory manual. Hibbitt, Karlsson and Sorensen Inc., 2007, Pawtucket, Rhode Island.

ABAQUS version 6.7, ABAQUS/CAE user's manual. Hibbitt, Karlsson and Sorensen Inc., 2007, Pawtucket, Rhode Island.

ABAQUS version 6.7, ABAQUS Keywords reference manual. Hibbitt, Karlsson and Sorensen Inc., 2007, Pawtucket, Rhode Island.

Benz, R, Niethammer, M S, Hurlebaus, S, and Jacobs, L J. Localization of notches with Lamb waves. Journal of the Acoustical Society of America 2003; 114(2):677-685.

Branham, S, Hurlebaus, S, Wilson, M, Beadle, B, Gaul, L. Nondestructive testing of overhead transmission lines. In: Conference on Damage in Composite Materials, CDCM 2006 Conference Proceedings 12, Stuttgart, Germany, 18th, 19th September 2006.

Greve, D W, Tyson, N L, Oppenheim, I J, Design and testing of lamb wave transducers. In: Proceedings of the 5th International Workshop on Structural Health Monitoring, 14th September 2005, Ed: Fu-Kuo Chang, 662-669.

Hurlebaus, S, Gaul, L, Smart structure dynamics. Mechanical Systems and Signal Processing, 2006; 20(2):255-281.

Hurlebaus, S, Niethammer, M, Jacobs, L J, Valle, C. Automated methodology to locate notches with lamb waves. Acoustics Research Letter Online 2001; 2(4):97-102.

Jamil, M, Thomas, M S, Moinuddin, L, Kumar, P. Improved scheme based on fuzzy logic for EHV transmission line protection. In: Proceedings of the 1999 11th International Symposium on 'High Voltage Engineering' 23-27th August 1999, London, England, IEE Conference Publication, 1, 467:1.360.P6-1.364.P6.

Khazem, D A, Kwun, H, Kim, S Y, Dynes, C. Long-range inspection of suspender ropes in suspension bridges using magnetostrictive sensor technology. Structural Health Monitoring – The Demands and Challenges, 2001; Ed. F.-K. Chang, CRC Press, Boca Raton, Florida

Kwun, H, Bartels, K A, Hanley, J J. Effect of tensile loading on the properties of elastic wave-propagation in a strand. Journal of Acoustical Society of America, 1998; 103:3370-3375.

Kwun, H. Teller, C M. Detection of fractured wires in steel cables using magnetostrictively sensors. Materials Evaluation, 1994; 52:503-507.

Moore, P J, Grace, D B. Remote sensing of overhead line conductor temperature using an infra-red sensor. In: 5th International Conference on Advances in Power System Control, Operation and Management, 2001, IEE Conference Publication, Lisbon, Portugal, 478 II:385-389.

Nishi, M, Sakurai, K, Taga, H, Yasumori, T, Matsushita, T, Hayashi, S. Improvements to the fault locating systems for the overhead power transmission lines. SEI Technical Review, 1999; 45:83-87.

Probert, S A, Song, Y H. Detection and classification of high frequency transients using wavelet analysis. In: Proceedings of the IEEE Power Engineering Society Transmission and Distribution Conference, Chicago, Illinois, 2002, 2:801-806.

Siegert, D, Brevet, P. Fatigue of stay cables inside end fittings: high frequencies of wind induced vibrations, OIPEEC Bulletin 2000, 89:43-51.

Urasawa, K, Kanemaru, K, Toyota, S, Sugiyama, K. New fault location system for power transmission lines using composite fiber-optic overhead ground wire (OPGW). IEEE Transactions on Power Delivery, 1989; 4(4):2005-2011.

Valle, C, Niethammer, M, Qu, J, Jacobs, L. Crack detection using guided circumferential waves. Journal of the Acoustical Society of America, 2001; 110:1282-1290.

VITA

Name Salil Subhash Kulkarni

Address Zachry Department of Civil Engineering

c/o Dr. Stefan Hurlebaus

Texas A&M University

College Station

Texas 77843-3136

Email: salil_kulkarni@neo.tamu.edu

Education B.Tech. (Structural) 2007 College of Engineering, Pune, India

M.S. (Structural) 2009 Texas A&M University, College Station